Interorbital singlet pairing in Sr2RuO4: A Hund's superconductor

Editors' Suggestion

Interorbital singlet pairing in Sr_2RuO_4: A Hund's superconductor

Stefan Käser,[1,2] Hugo U. R. Strand,[3,4,5] Nils Wentzell,[5] Antoine Georges,[6,5,7,8] Olivier Parcollet,[5,9] and Philipp Hansmann[10,2]

[1]*Max-Planck-Institut für Festkörperforschung, Heisenbergstrasse 1, 70569 Stuttgart, Germany*
[2]*Department of Physics, Friedrich-Alexander Universität Erlangen-Nürnberg, 91058, Erlangen, Germany*
[3]*School of Science and Technology, Örebro University, Fakultetsgatan 1, SE-701 82, Örebro, Sweden*
[4]*Department of Physics, Chalmers University of Technology, SE-412 96 Gothenburg, Sweden*
[5]*Center for Computational Quantum Physics, Flatiron Institute, Simons Foundation, 162 5th Ave., New York, New York 10010, USA*
[6]*Collège de France, 11 place Marcelin Berthelot, 75005 Paris, France*
[7]*CPHT, CNRS, Ecole Polytechnique, IP Paris, F-91128 Palaiseau, France*
[8]*DQMP, Université de Genève, 24 quai Ernest Ansermet, CH-1211 Geneva, Switzerland*
[9]*Université Paris-Saclay, CNRS, CEA, Institut de Physique Théorique, 91191, Gif-sur-Yvette, France*
[10]*Max-Planck-Institut für Chemische Physik fester Stoffe, Nöthnitzerstrasse 40, 01187 Dresden, Germany*

(Received 19 July 2021; accepted 16 March 2022; published 1 April 2022)

We study the superconducting gap function of Sr_2RuO_4. By solving the linearized Eliashberg equation with a correlated pairing vertex extracted from a dynamical mean-field calculation we identify the dominant pairing channels. An analysis of the candidate gap functions in orbital and quasiparticle band basis reveals that an interorbital singlet pairing of even parity is in agreement with experimental observations. It reconciles in particular the occurrence of a two-component order parameter with the presence of line nodes of quasiparticles along the *c* axis in the superconducting phase. The strong angular dependence of the gap along the Fermi surface is in stark contrast to its quasilocality when expressed in the orbital basis. We identify local interorbital spin correlations as the driving force for the pairing and thus reveal the continuation of Hund's physics into the superconducting phase.

DOI: 10.1103/PhysRevB.105.155101

I. INTRODUCTION

Since its discovery 27 years ago [1], the superconducting ground state of Sr_2RuO_4 remains a major challenge in strongly correlated electron physics [2,3]. The symmetry of the order parameter is still a debated question, with recent experiments challenging established views [4,5] (for recent reviews and discussion see, e.g., [6–8]).

In the normal state, material-realistic calculations combining density-functional theory (DFT) and dynamical mean-field theory (DMFT [9,10]) have been able to explain, on a microscopic level, many experimental observations. This includes the emergence of quasiparticles with anisotropic mass renormalization when cooling down from the incoherent high-temperature phase to the Hund's metal Fermi-liquid regime [11] as well as quasiparticle dispersions and the subtle reshaping of the Fermi surface due to the spin-orbit coupling as probed by photoemission experiments [12]. More recently, momentum-resolved static magnetic susceptibilities computed in DMFT [13–15] have been shown to agree well with inelastic neutron-scattering experiments [16], when vertex corrections are properly taken into account [13,14]. These recent works highlight the correlated nature of Sr_2RuO_4 as a Hund's metal [17] and the importance of local spin fluctuations, as in other Hund's metals like the iron-based superconductors [18–21].

In contrast with the normal state, the nature of the low-temperature superconducting state of Sr_2RuO_4 remains a matter of intense debate today. Despite a large body of experiments, no consensus has been reached, for example, on the precise form and symmetry of the superconducting order. The difficulty comes from the multiorbital nature of this material and the spin-orbit coupling (SOC), which yields a large number of possible pairing symmetries (see Ref. [22] for a classification based on group theory). This makes a direct phenomenological approach difficult, in which one considers every possible pairing authorized by symmetry and finds the (hopefully) unique one compatible with every experiment. Several works have been published in this direction (see, e.g., [8,23,24]).

In this work, we instead use microscopic computations at high temperature, in the normal-state Hund's metal regime, to guide us towards the most likely superconducting order candidate. We directly solve the linearized Eliashberg equation for superconductivity from high temperatures, nonperturbatively, without any assumption on the symmetry of the order

parameter, for the same realistic model used in the successful studies on the normal state. We identify two dominant channels in the Eliashberg analysis. Both are *two-component spin-singlet* modes. The first one has *inter*orbital character, even momentum symmetry, and odd orbital symmetry, while the second has *intra*orbital character and odd momentum symmetry. We will show, however, that the *inter*orbital channel is the only one compatible with experiments. This kind of pairing was not identified in similar previous studies that used a random phase approximation (RPA) like approximation [25] or a self-consistent GW + DMFT approach [15].

This paper is organized as follows. In Sec. II, we present our model, based on realistic electronic structure; in Sec. III, we present our formalism and discuss every approximation we make in this work at a general level; in Sec. IV, we discuss our numerical results and the two dominant superconducting symmetry channels and compare to previous related works [15,25]; in Sec. V, we present a detailed comparison of these two pairing states to experiments; finally, we conclude in Sec. VI.

II. MODEL

The structure of Sr_2RuO_4 is that of an undistorted layered perovskite with $D4h$ tetragonal point-group symmetry on the Ru sites. Due to the strong induced cubic crystal-field splitting of the Ru-4d states ($10Dq = E_{e_g} - E_{t_{2g}}$) the e_g states are pushed well above the Fermi level. Hence, the three bands crossing the Fermi level can be represented by a localized Wannier-orbital basis transforming as the Ru-4d-t_{2g} orbitals xy, xz, and yz, with a nominal filling of four valence electrons. While the tetragonal onsite splitting of these orbitals is rather small, $E_{xy} - E_{xz/yz} \approx 80$ meV, the hopping parameters are remarkably anisotropic showing a two-dimensional (2D) like dispersion for xy states and one-dimensional (1D) dispersion for xz and yz bands, respectively. This can also be seen in the Fermi-surface (FS) topology where the xz and yz states form nearly one-dimensional Fermi-surface sheets, that hybridize weakly and give rise to the hole pocket α (centered around X) and the electron pocket β (centered around Γ). For resolved orbital contributions of xz and yz states, see the color-coded lower panel of Fig. 1. The in-plane xy states, on the other hand, are dominant in the formation of the electron pocket γ (concentric with β) [see Fig. 1 (upper panel)].

Aside from $D4h$ hopping and crystal-field potential, spin-orbit-coupling (SOC) effects are sizable for the Ru-4d valence electrons and play an important role in Sr_2RuO_4 [26,27]. For the three-band t_{2g} low-energy model it has been shown that the effect of SOC can be captured using a local $\mathbf{l}\cdot\mathbf{s}$ operator and that the effective spin-orbit coupling is enhanced by correlations [12,28,29]. Its effects within the t_{2g} subspace have significant impact in large parts of the Brillouin zone (BZ) around the Fermi level and, more specifically, the shape *and orbital character* of the Fermi surface at the points where the Fermi-surface sheets α, β, and γ are in close proximity [12], e.g., along Γ-X in Fig. 1.

In this study the normal-state electronic structure of Sr_2RuO_4 is described using an *ab initio* derived low-energy t_{2g} effective model, computed using density-functional theory (DFT) and a Wannierization of the three Kohn-Sham bands

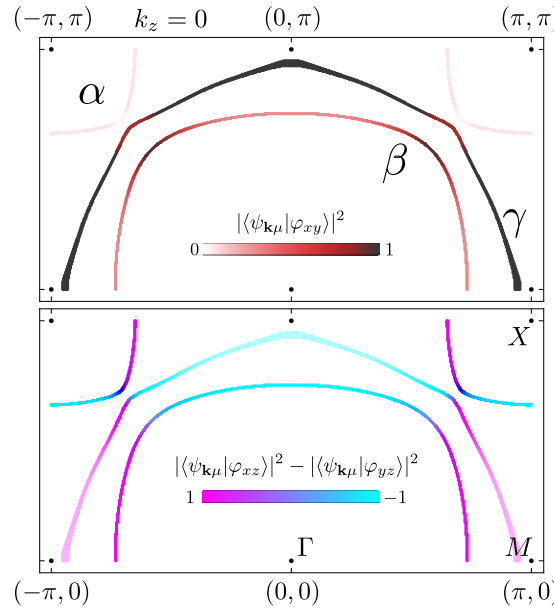

FIG. 1. Plot of the orbital character of the Fermi surface in the k_x, k_y plane at $k_z = 0$, including spin-orbit coupling. The in-plane xy orbital dominates the γ Fermi-surface sheet (top) while the out-of-plane orbitals xz and yz dominate the outer α hole pocket and the inner β electron pocket (bottom).

crossing the Fermi level. The model has been used in several previous studies [11,12,14]; for details on the model construction using WIEN2K [30] and WANNIER90 [31] we refer to Ref. [12]. The effective screened Coulomb interaction was modeled using the rotationally invariant Kanamori form projected on the t_{2g} subspace, and parametrized by a Hubbard U and a Hund's J. The interaction parameters $U = 2.3$ eV and $J = 0.4$ eV are set in accordance with previous studies, which have correctly reproduced quantum oscillation experiments [11], angle-resolved photoemission spectroscopy [12], and the momentum-dependent static spin response function [14].

III. FORMALISM

In order to study the superconducting instability in Sr_2RuO_4, we solve the linearized Eliashberg equation in all possible symmetry channels. We use a DMFT-based approximation detailed below to approximate the two-body quantities involved in this equation. A more conventional approach to study superconductivity in (cluster) DMFT would be to directly solve the DMFT equations for a single site or a small cluster in the ordered phase, or to compute the superconducting susceptibility above T_c from the linear response of *one-body* quantities to a small pairing field. This is well known in, e.g., the study of s-wave or d-wave superconducting orders in attractive or repulsive Hubbard model (see, e.g., [32]). The Eliashberg approach has the advantage of being able to describe an arbitrary momentum dependence of the superconducting gap function Δ, a very important question that can not be addressed with cluster DMFT methods. However, this flexibility comes at a cost: a limitation to high temperatures and the need to rely on approximations for two-body quantities which are only partially controlled.

In this section, we first define the generalized propagators and self-energies in a Nambu basis as well as their symmetry properties. Then, we present the Eliashberg equation and the relevant Parquet and Bethe-Salpeter equations for the vertex. Finally, we discuss in detail our approximation strategy and the role of spin-orbit coupling for our results.

A. Generalized propagators and self-energies

First, we define the anomalous Green's functions at imaginary time τ and momentum $\mathbf{k}$ by

$$F^{\sigma\sigma'}_{ab}(\mathbf{k},\tau) \equiv \langle \mathcal{T}_\tau c_{a\sigma}(\mathbf{k},\tau) c_{b\sigma'}(-\mathbf{k},0)\rangle, \tag{1}$$

$$\overline{F}^{\sigma\sigma'}_{ab}(\mathbf{k},\tau) \equiv \langle \mathcal{T}_\tau c^\dagger_{a\sigma}(\mathbf{k},\tau) c^\dagger_{b\sigma'}(-\mathbf{k},0)\rangle, \tag{2}$$

where $\mathcal{T}_\tau$ is the time-ordering operator and $c_{a\sigma}(\mathbf{k},\tau)$ $[c^\dagger_{a\sigma}(\mathbf{k},\tau)]$ are fermionic annihilation (creation) operators in the Heisenberg representation with orbital (a, b) and spin $(\sigma, \sigma' \in \{\uparrow,\downarrow\})$ indices. In a Nambu basis spanned by the spinors

$$\mathbf{\Psi}_a(\mathbf{k},\tau) \equiv (c_{a\uparrow}(\mathbf{k},\tau), c_{a\downarrow}(\mathbf{k},\tau), c^\dagger_{a\uparrow}(-\mathbf{k},\tau), c^\dagger_{a\downarrow}(-\mathbf{k},\tau)), \tag{3}$$

the anomalous propagators are the block-off-diagonal entries of the generalized single-particle propagator

$$\begin{aligned}\hat{\mathbf{G}}_{ab}(\mathbf{k},\tau) &\equiv -\langle \mathcal{T}_\tau \mathbf{\Psi}_a(\mathbf{k},\tau)\mathbf{\Psi}^\dagger_b(\mathbf{k},0)\rangle \\ &= \begin{pmatrix} \mathbf{G}_{ab}(\mathbf{k},\tau) & -\mathbf{F}_{ab}(\mathbf{k},\tau) \\ -\overline{\mathbf{F}}_{ab}(\mathbf{k},\tau) & \overline{\mathbf{G}}_{ab}(\mathbf{k},\tau)\end{pmatrix}.\end{aligned} \tag{4}$$

In this equation, $\mathbf{G}$ and $\mathbf{F}$ are 2×2 matrices in spin space. The diagonal entries are the normal single-particle (single-hole) propagators $\mathbf{G}_{ab}(\mathbf{k},\tau)$ $[\overline{\mathbf{G}}_{ab}(\mathbf{k},\tau)]$. After Fourier transforming from imaginary time to Matsubara frequency, the generalization of the corresponding Dyson equation reads as

$$\hat{\mathbf{G}}(\mathbf{k}, i\nu_n) = \hat{\mathbf{G}}^0(\mathbf{k}, i\nu_n) + \hat{\mathbf{G}}^0(\mathbf{k}, i\nu_n)\mathbf{\Sigma}(\mathbf{k}, i\nu_n)\hat{\mathbf{G}}(\mathbf{k}, i\nu_n), \tag{5}$$

where

$$\hat{\mathbf{G}}^0_{ab}(\mathbf{k}, i\nu_n) = \begin{pmatrix} \mathbf{G}^0_{ab}(\mathbf{k}, i\nu_n) & 0 \\ 0 & \overline{\mathbf{G}}^0_{ab}(\mathbf{k}, i\nu_n)\end{pmatrix} \tag{6}$$

is the noninteracting generalized propagator and

$$\mathbf{\Sigma}_{ab}(\mathbf{k}, i\nu_n) = \begin{pmatrix} \mathbf{\Sigma}^{\text{norm}}_{ab}(\mathbf{k}, i\nu_n) & \mathbf{\Delta}_{ab}(\mathbf{k}, i\nu_n) \\ \overline{\mathbf{\Delta}}_{ab}(\mathbf{k}, i\nu_n) & \overline{\mathbf{\Sigma}}^{\text{norm}}_{ab}(\mathbf{k}, i\nu_n)\end{pmatrix} \tag{7}$$

defines the generalized self-energy. As for the Green's function $\hat{\mathbf{G}}$, the diagonal blocks in the self-energy, $\mathbf{\Sigma}^{\text{norm}}$ and $\overline{\mathbf{\Sigma}}^{\text{norm}}$, are the single-particle and single-hole self-energies and the off-diagonal pairing term Δ is called *the superconducting gap function*. While Δ in principle only is finite in the symmetry-broken superconducting state, it is possible to determine the superconducting instability in terms of Δ directly from the normal phase using the linearized Eliashberg formalism.

B. Eliashberg and Parquet equations

The linearized Eliashberg equation for the superconducting gap function Δ reads as [25,33–35]

$$\begin{aligned}\lambda \Delta^{s/t}_{ab}(K) = &-\frac{1}{2N_{\mathbf{k}}\beta}\sum_{K'} \Gamma^{s/t}_{cadb}(Q=0,K',K) \\ &\times G_{cf}(-K')G_{de}(K')\Delta^{s/t}_{ef}(K'),\end{aligned} \tag{8}$$

where $\Gamma^{s/t}$ is the irreducible vertex function in the singlet/triplet channel, G is the spin-independent (interacting) single-particle lattice Green function, Q (K) is the bosonic (fermionic) four-vector consisting of Matsubara frequency (ω_n/ν_n) and momentum $(\mathbf{q}/\mathbf{k})$, $N_{\mathbf{k}}$ is the number of momenta, and β is the inverse temperature. Here all latin indices are orbital indices and the Einstein summation convention is used.

The Eliashberg equation [Eq. (8)] is an eigenvalue problem with eigenvectors Δ and eigenvalues λ. When lowering the temperature, the superconducting instability occurs at the critical temperature T_c, at which the eigenvalue λ of the dominant eigenvector gap function Δ reaches unity. In practice, because our numerical solution is limited to high and intermediate temperatures, we are not able to reach T_c, but we will rather compare the evolution of the 10 largest eigenvalues λ and the corresponding eigenvector gap functions Δ as a function of temperature.

In this paper, we neglect the spin-orbit contributions to the pairing vertex, which allows us to solve Eq. (8) separately for singlet (s) and triplet (t) channels in the spin-diagonalized form [36,37], i.e.,

$$\Delta^s_{ab} = \Delta^{\uparrow\downarrow}_{ab} - \Delta^{\downarrow\uparrow}_{ab}, \quad \Gamma^s_{abcd} = \Gamma^{\uparrow\uparrow\downarrow\downarrow}_{abcd} - \Gamma^{\uparrow\downarrow\downarrow\uparrow}_{abcd}, \tag{9}$$

and

$$\begin{aligned}\Delta^t_{ab} &= \Delta^{\uparrow\downarrow}_{ab} + \Delta^{\downarrow\uparrow}_{ab} = \Delta^{\uparrow\uparrow}_{ab} = \Delta^{\downarrow\downarrow}_{ab}, \\ \Gamma^t_{abcd} &= \Gamma^{\uparrow\uparrow\downarrow\downarrow}_{abcd} + \Gamma^{\uparrow\downarrow\downarrow\uparrow}_{abcd} = \Gamma^{\uparrow\uparrow\uparrow\uparrow}_{abcd} = \Gamma^{\downarrow\downarrow\downarrow\downarrow}_{abcd}.\end{aligned} \tag{10}$$

The irreducible vertex $\Gamma^{s/t}$ can be computed from the fully irreducible vertex Λ and the reducible vertex $\Phi^{d/m}$ through the Parquet equation [36–38]. The irreducible singlet vertex Γ^s is given by

$$\begin{aligned}\Gamma^s_{abcd}(Q,K,K') = &-\Lambda^s_{abcd}(Q,K,K') \\ &+\left[\tfrac{3}{2}\Phi^m_{abcd} - \tfrac{1}{2}\Phi^d_{abcd}\right](Q-K-K',K,K') \\ &+\left[\tfrac{3}{2}\Phi^m_{cbad} - \tfrac{1}{2}\Phi^d_{cbad}\right](K-K',Q-K,K'),\end{aligned} \tag{11}$$

and the irreducible triplet vertex Γ^t by

$$\begin{aligned}\Gamma^t_{abcd}(Q,K,K') = &\Lambda^t_{abcd}(Q,K,K') \\ &+\left[\tfrac{1}{2}\Phi^m_{abcd} + \tfrac{1}{2}\Phi^d_{abcd}\right](Q-K-K',K,K') \\ &-\left[\tfrac{1}{2}\Phi^m_{cbad} + \tfrac{1}{2}\Phi^d_{cbad}\right](K-K',Q-K,K'),\end{aligned} \tag{12}$$

where the superscript d/m indicates the density/magnetic channel [38] $\Phi^{d/m}_{abcd} = \Phi^{\uparrow\uparrow\uparrow\uparrow}_{abcd} \pm \Phi^{\uparrow\uparrow\downarrow\downarrow}_{abcd}$.

The reducible vertex function $\Phi^{d/m}$ is related to $\Gamma^{d/m}$ the irreducible vertex function in the density/magnetic

channel by

$$\Phi^{d/m}_{abcd}(Q,K,K') = \frac{1}{(N_{\mathbf{k}}\beta)^2}\sum_{P_1,P_2}\Gamma^{d/m}_{abef}(Q,K,P_1) \times \chi^{d/m}_{fegh}(Q,P_1,P_2)\Gamma^{d/m}_{hgcd}(Q,P_2,K'). \quad (13)$$

Here, $\chi^{d/m}$ is the generalized susceptibility, obtained by solving the Bethe-Salpeter equation

$$\chi^{d/m}_{abcd}(Q,K,K') = \chi^{0,d/m}_{abcd}(Q,K,K') + \frac{1}{(N_{\mathbf{k}}\beta)^2}\sum_{P_1P_2}\chi^{0,d/m}_{abef}(Q,K,P_1) \times \Gamma^{d/m}_{fegh}(Q,P_1,P_2)\chi^{d/m}_{hgcd}(Q,P_2,K'), \quad (14)$$

where $\chi^{0,d/m}$ is the bare lattice "bubble":

$$\chi^{0,d/m}_{abcd}(Q,K,K') \equiv -N_{\mathbf{k}}\beta G_{da}(K)G_{bc}(K+Q)\delta_{K,K'}. \quad (15)$$

C. Approximation strategy

The Eliashberg and Parquet equations written above are exact, but untractable. Hence, we develop an approximation based on the DMFT solution of this material. Let us first emphasize the central role played in these equations by the magnetic susceptibility χ^m, as we see in Eq. (13). In Ref. [14], χ^m has been studied for this material in great details within the DMFT approximation, *including vertex corrections*. An excellent agreement with experiments was obtained, but only if vertex corrections were included through the Bethe-Salpeter equation [Eq. (14)]. Our approximation strategy consists therefore in using the full DMFT generalized susceptibility $\chi^{d/m}_{abcd}$ in Eq. (13) (with vertex corrections) and approximate the other vertices Λ and Γ with simple static (effective) approximations.

More precisely, we first approximate the fully irreducible vertex Λ by its bare value $\tilde{\Lambda}$

$$\Lambda \approx \tilde{\Lambda} \quad (16)$$

whose exact form is given in Appendix G as a function of U and J.

Second, we approximate $\Gamma^{d/m}$ by a static effective interaction. Conceptually, we could use here the DMFT impurity vertex $\Gamma^{d/m}_{\mathrm{DMFT}}$, but as explained in details in Appendix H, we replace it by an effective static approximation which reproduces well the low-energy behavior of Γ^s. This is necessary in practice because of the stochastic noise in Λ and Γ in the hybridization expansion quantum Monte Carlo (CT-HYB) [39–42] solver we use here to solve the DMFT self-consistent impurity model.

D. Role of spin-orbit coupling

As has been pointed out in previous works (e.g., [26,27]) and as mentioned in Sec. II, spin-orbit coupling affects the shape and orbital character of the Fermi surface significantly. In its presence, spin ceases to be a good quantum number for the quasiparticles around ε_F, the anomalous propagators of the superconducting phase equations (1) and (2) are not diagonal in the spin eigenbasis, and Cooper pairs cannot be classified as either singlet or triplet. Moreover, the strong momentum dependence of the SOC entanglement prohibits any transform to a local pseudospin for recovery of singlet and triplet notion (different, e.g., from the local $\mathbf{J}^2$, J_z basis in Ce-based heavy-fermion superconductors).

While there have been weak coupling studies that include spin-orbit coupling [43–45] on the level of the pairing vertex, including SOC in our nonperturbative approach on the level of the Parquet equations (11) and (12) is currently not feasible in practice. We therefore employ an approximation strategy, which has previously been successfully applied for the calculation of the magnetic response [14] and neglect SOC on the level of the two-particle vertices. This means that our anomalous self-energy Δ [Eq. (7)] *can be classified as singlet or triplet* in nature. For the anomalous propagator $\mathbf{F}$, however, the SOC entanglement enters via the normal-state propagator $\mathbf{G}^0$ [Eq. (6)].

IV. RESULTS

A. Solutions of the Eliashberg equation

A finite superconducting gap is indicated by an eigenvalue $\lambda_i \geqslant 1$ in the linearized Eliashberg equation (8). For the considered temperatures, all solutions of our scheme yield $\lambda_i < 1$, which is expected. Nonetheless, the λ_i eigenvalues above T_c serve as indicators for potentially dominating gap symmetries at lower temperatures and at T_c. Hence, we sort the gap functions in descending order for the calculated temperatures. We further classify them by their (anti)symmetry upon permuting spin, parity, orbital, and time indices:

$$\hat{S}\Delta^{\sigma\sigma'}_{ab}(i\nu,\mathbf{k}) = \Delta^{\sigma'\sigma}_{ab}(i\nu,\mathbf{k}), \quad (17a)$$

$$\hat{P}\Delta^{\sigma\sigma'}_{ab}(i\nu,\mathbf{k}) = \Delta^{\sigma\sigma'}_{ab}(i\nu,-\mathbf{k}), \quad (17b)$$

$$\hat{O}\Delta^{\sigma\sigma'}_{ab}(i\nu,\mathbf{k}) = \Delta^{\sigma\sigma'}_{ba}(i\nu,\mathbf{k}), \quad (17c)$$

$$\hat{T}\Delta^{\sigma\sigma'}_{ab}(i\nu,\mathbf{k}) = \Delta^{\sigma\sigma'}_{ab}(-i\nu,\mathbf{k}), \quad (17d)$$

where a, b are orbital and σ, σ' are spin indices. The overall antisymmetry of the gap function which is dictated by the Pauli principle is usually formalized as the "*SPOT*" condition [25,46–48]

$$\hat{S}\hat{P}\hat{O}\hat{T}\Delta^{\sigma\sigma'}_{ab}(i\nu,\mathbf{k}) = -\Delta^{\sigma\sigma'}_{ab}(i\nu,\mathbf{k}) \quad (18)$$

and, by construction, fulfilled by our gap functions. In Table I (which contains the gaps resolved *SPOT* symmetry) we summarize our results for the 10 gap functions with the highest λ eigenvalues.[1]

In Fig. 2 the temperature dependence is highlighted which motivates our identification of prime candidates for the gap function in Sr_2RuO_4. At the lowest calculated temperatures, we find the largest λ eigenvalue for a doubly degenerate interorbital (xy-xz, xy-yz) singlet. As it is the highest singlet with the second highest temperature gradient (red points in in Fig. 2) we will consider this interorbital gap function (from

[1]This choice is motivated by the fact that the $d_{x^2-y^2}$ singlet gap function, which is leading in weak-coupling theory (see Appendix K), dropped down to position 10 in our nonperturbative scheme.

TABLE I. The 10 leading gap functions in descending order at $T \approx 290$ K (cf. Fig. 2). Our considered prime candidates $\Delta^{i.o.}$ and Δ^{f} are highlighted in gray. Gaps with the same *SPOT* symmetry share the same color. As many of our gap functions have not only a single finite matrix element in the orbital space the column "Orbital character" indicates the dominant orbital matrix element (see also Fig. 3).

	Symmetries				
Pairing	Spin	Parity	Orbital	Time	Orbital character
Interorbital singlet $\Delta^{i.o.}$	−	+	−	−	degenerate {inter xy-yz, interxy-xz}
Interorbital triplet	+	+	−	+	degenerate {inter xy-yz, inter xy-xz}
xz-yz interorbital triplet	+	+	−	+	inter xz-yz
xy triplet	+	+	+	−	intra xy
xz-yz interorbital singlet	−	+	−	−	inter xz-yz
xy triplet 2	+	+	+	−	intra xy
$d_{x^2-y^2}$ triplet	+	+	+	−	intra xz/yz
f-wave singlet Δ^{f}	−	−	+	−	degenerate {intra xz, intra yz}
Extended s-wave singlet	−	+	+	+	intra xz/yz
$d_{x^2-y^2}$ singlet	−	+	+	+	intra xz/yz

now on referred to as $\Delta^{i.o.}$) as our first principal candidate. As a second candidate we identify a doubly degenerate intraorbital (xz and yz) f-wave singlet (Δ^{f}) which shows the overall strongest temperature gradient (green line in Fig. 2). In Fig. 3 we plot both components of $\Delta^{i.o.}$ (a) and Δ^{f} (b) as a matrix of their orbital indices. Each matrix element of the plot shows, as a color map, the momentum dependence of the corresponding gap function with respect to k_x and k_y in the $k_z = 0$ plane. From these plots we understand directly the twofold degeneracy of both gap functions as their components are transformed into one another upon the tetragonal symmetry $\pi/2$ rotation around the k_z axis. The orbital and momentum dependence of $\Delta^{i.o.}$ and Δ^{f} is, however, completely different.

$\Delta^{i.o.}$ is odd under permutation of orbital indices but has even parity. Most remarkable, however, is its very weak $\mathbf{k}$ dependence of the dominant matrix elements (i.e., $\mathrm{Re}[\Delta^{i.o.}_{xy-xz}]$ and $\mathrm{Re}[\Delta^{i.o.}_{xy-yz}]$) which displays a variation of less than 10% around its mean value in the BZ. To quantify this, we plot in Fig. 4(a) the $\mathbf{k}$ dependence of the dominant matrix elements of real and imaginary parts of the gap function along a high-symmetry path in the BZ for the three temperatures of our calculation. (Due to symmetry relations, we only need one plot for each real and imaginary part.) The remarkably weak $\mathbf{k}$ dependence of $\Delta^{i.o.}$ in the orbital basis suggests a rather local pairing mechanism. If there is not a dramatic increase of $\mathbf{k}$ dependence at lower T, this is a promising outlook for DMFT studies. Computing the superconducting susceptibility by application of an interorbital pairing field would allow for an extrapolation to the lowest temperatures and eventually an estimate of T_c.

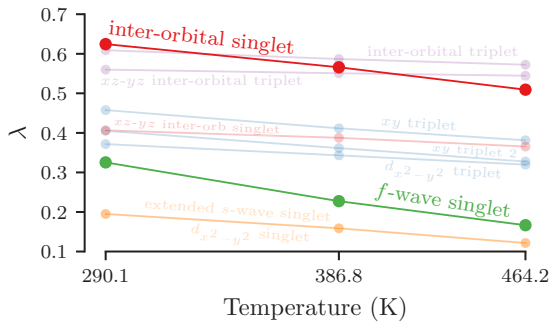

FIG. 2. Plot of the temperature-dependent Eliashberg λ eigenvalues for the 10 gap functions closest to $\lambda = 1$. We highlight the two selected prime candidates, an interorbital singlet (red) and an f-wave singlet (green), for our further analysis.

We now turn to Δ^{f} which is orbitally practically diagonal. It is even with respect to orbital index permutations but, as the name suggests, odd in parity. It shows several horizontal nodal lines in the BZ. Its strong $\mathbf{k}$ dependence can be seen in detail in Fig. 4(b) and suggests a much more nonlocal pairing in real space. Because of this strong momentum dependence, the direct study of this pairing state in the superconducting state with cluster DMFT methods would require impractically large cluster sizes. We stress here that the plots in Fig. 3 are shown in the *orbital basis* and must not be superimposed with the Fermi surfaces which are strongly mixed in their orbital character (see Fig. 1).

Finally, we remark upon the odd-frequency symmetry shown by both of our candidate gap functions. Odd-ω superconductivity has indeed been the focus of previous works. Early works focused on controversies regarding the thermodynamic stability [49,50] as well as the nature of the Meissner effect (i.e., diamagnetic or paramagnetic) [51] of such a phase. Today we know that odd-ω superconductivity can exist as it was realized experimentally in superconductor-ferromagnet junctions [52] or [53]. In contrast to the single-band case there is no generic issue with the thermodynamic stability of multiorbital systems with ω-odd components in the anomalous propagator $F(\omega)$, as explicitly shown on a mean-field level in Ref. [54] with a static anomalous self-energy Δ. Proposed material candidates for bulk multiorbital odd-ω superconductivity include the heavy-fermion compound UPt_3, buckled-honeycomb materials, and Sr_2RuO_4 [55,56]. However, in multiorbital systems the notion of odd-frequency superconductivity needs to be defined more precisely. The

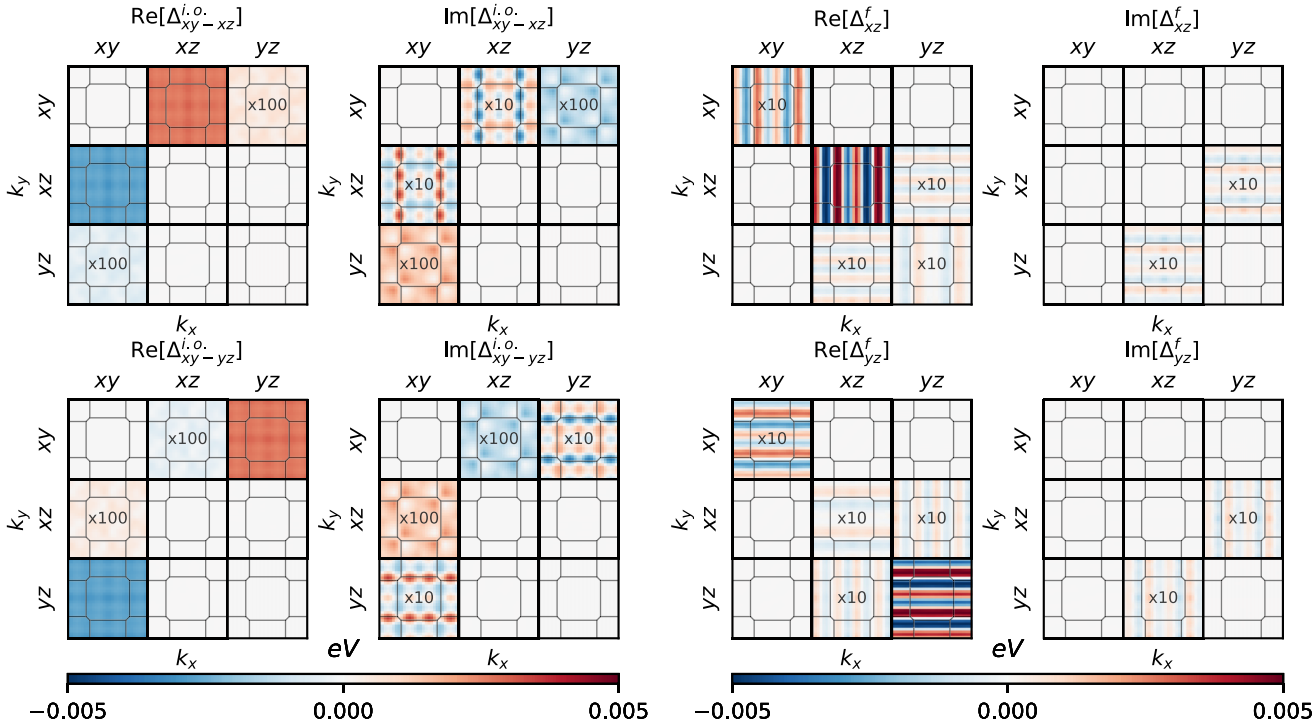

(a) The two degenerate inter-orbital singlets $\Delta^{i.o.}_{xy-xz}$, $\Delta^{i.o.}_{xy-yz}$ in the orbital basis

(b) The two degenerate f-wave singlets Δ^{f}_{xz}, Δ^{f}_{yz} in the orbital basis

FIG. 3. Momentum dependence of the gap functions $\Delta_{ab}(k_x, k_y, k_z = 0, iv_0)$ in the t_{2g} orbital basis, $a, b \in \{xz, yz, xy\}$ at the first Matsubara frequency iv_0. Each entry of the matrices displays the momentum dependence as a function of (k_x, k_y) in the Brillouin zone. The real and imaginary components are shown separately for (a) the degenerate interorbital singlet gaps $\Delta^{i.o.}_{xy-xz}$ and $\Delta^{i.o.}_{xy-yz}$ with only orbital off-diagonal contributions, and (b) the degenerate intraorbital f-wave singlet gaps $\Delta^{i.o.}_{zx}$ and $\Delta^{i.o.}_{yz}$. (Small orbital components are scaled with the scaling factors shown in the respective orbital component panel.)

generalized Dyson equation (5) is a matrix equation in the orbital indices and can give rise to an anomalous propagator $F(\omega)$ with both ω-even *and* ω-odd components in multiple ways. More specifically, ω-odd components in $F(\omega)$ occur in systems with interorbital hybridization, interorbital anomalous self-energy, or ω-odd components in the anomalous self-energy $\Delta(\omega)$, as well as any combination thereof. In particular, the interorbital singlet pairing calculated here for Sr_2RuO_4 has a combination of all of the above.

At the end of this section, as there have been previous theoretical studies of pairing in Sr_2RuO_4 using the Eliashberg approach, we put our results into context of these previous works. Some of the gaps listed as solutions in Table I have been discussed as potential candidates for Sr_2RuO_4 in the context of an RPA like approximation [25] (which we reproduce

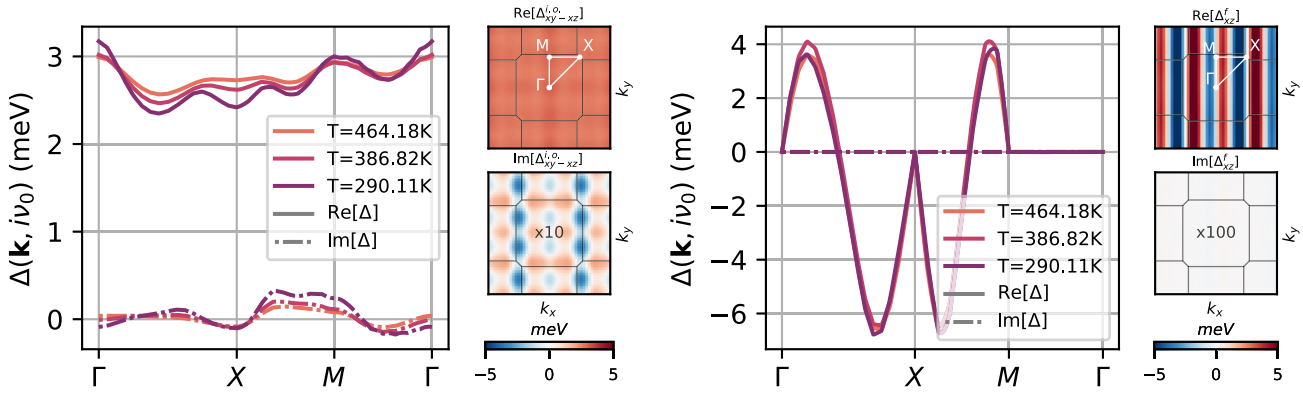

(a) The $xy - xz$ component of the inter-orbital singlet gap function.

(b) The $xz - xz$ component of the f-wave singlet gap function.

FIG. 4. High-symmetry k-space paths for the dominating orbital components in the two candidate gap functions for three temperatures. The k-space plane cuts are for the intermediate temperature and equivalent to Fig. 3.

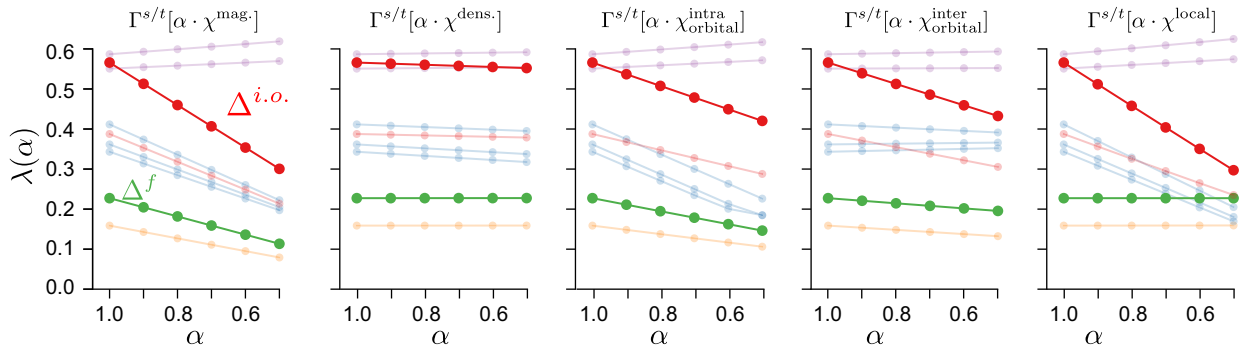

FIG. 5. Dependence of the Eliashberg λ eigenvalues at $T \approx 386$ K on the scaling factor α tuning different fluctuation channels in the pairing vertex.

in Appendix K). The overall discrepancy between our results and such a weak-coupling approach is expected, however, as vertex corrections strongly affect the pairing mechanism (see next section). Indeed, it has been shown [14] that including the full vertex when calculating the momentum-dependent magnetic response function yields a much better agreement with neutron-scattering experiments [16] and corrects some of the significant discrepancies found at the RPA level. The closest study to our approach is a self-consistent *GW* + DMFT [15] study with which we have, despite differences in the approximations, an overall good agreement. The dominant pairing states that we find in this work were, however, not identified or addressed in Ref. [15], which we attribute to the symmetry constraints imposed in that study.

We stress that our results are obtained above T_c and should be understood as a *proposal* for possible gap symmetry and pairing mechanism in Sr_2RuO_4 and not as an "*ab initio* prediction." Indeed, we cannot judge with certainty how the eigenvalues will change at lower temperatures and if, e.g., the f-wave singlet will surpass the interorbital singlet. As we will show later, however, comparison to the large amount of experimental evidence lets us conclude that the interorbital singlet gap can be (i) reconciled with all experiments and (ii) could even help to explain an unsolved puzzle in quasiparticle interference (QPI) experiments [57].

B. Channel analysis

In order to shed further light on the pairing mechanism of the gap functions reported in Table I we perform a "channel analysis" to determine which two-particle correlators drive the pairing for each of the gap functions. To do this, we downscale selected components of the lattice susceptibility which enters the equation for the pairing vertices (11) and (12). Specifically, we distinguish between magnetic, density, interorbital and intraorbital, and local fluctuations. For details, see Appendix J. Keeping the original gap functions fixed, we compute new λ values with the modified pairing vertices $\Gamma^{s/t}$. The results for $T \approx 386$ K are shown in Fig. 5. Concentrating on our prime candidates $\Delta^{i.o.}$ and Δ^{f}, we note that both are mainly driven by spin fluctuations. Especially, $\Delta^{i.o.}$ seems to be strongly driven by magnetic fluctuations and, more specifically, by local magnetic interorbital and intraorbital correlations. Given that these correlations dominate also the Hund's metallic normal state, it seems plausible that a superconducting gap function driven by such correlations turns out to have a large Eliashberg eigenvalue. We note that superconductivity due to local spin fluctuations in the context of Hund's metals has been studied in a different context, e.g., in Ref. [58] in relation to spin-triplet pairing and in Ref. [59] in relation to the non-Fermi-liquid spin dynamics of Hund's metals (which, however, does not apply to Sr_2RuO_4 in the Fermi-liquid regime). The relevance of Hund's driven orbital entanglement has recently also been emphasized for the superconducting state of twisted bilayer graphene and a "harmonic fingerprint" analysis proposed to analyze the orbital composition of the pairing state [60].

V. COMPARISON TO EXPERIMENTS

The pairing mechanism and symmetry of the superconducting order parameter of Sr_2RuO_4 are still outstanding open questions, despite 27 years of intense experimental and theoretical investigations [7]. New perspectives have recently entirely transformed this field, with the discovery by Pustogow *et al.* [4] (see also [5]) that the Knight shift actually sharply drops upon crossing T_c, hence challenging the triplet-pairing (odd-parity) interpretation. For recent discussions and reviews see, e.g., Refs. [6,8,57,61,62].

In this section, we critically examine whether our theoretical findings are consistent with available experimental evidence, focusing on the two main challengers: the interorbital singlet and the f-wave singlet (see Table I). As shown below, we conclude that the interorbital singlet gap is in agreement with basically all experiments, in contrast to the f-wave singlet which is ruled out by the momentum distribution of Bogoliubov QPI measurements.

A. Spin character and two-component gap

Our two candidate gap functions are both singlets. This is in agreement with the recent NMR finding that the Knight shift drops upon crossing T_c [4,5], which rules out triplet gaps with an out-of-plane d vector.

They also both correspond to a two-component order parameter, i.e., transforming under a two-dimensional representation with E symmetry. This is in agreement with recent ultrasound measurements which revealed a jump in the c_{66} elastic constant, a finding which is only consistent with a two-dimensional representation [63,64] (see, however,

[8] for an alternative proposal involving two near-degenerate components rather than a symmetry-imposed degeneracy). Muon spin-resonance (μSR) experiments also point at a two-component order parameter [62], and the most recent μSR experiments under hydrostatic pressure further suggest a symmetry-imposed degeneracy [65].

B. Time-reversal symmetry

From our two-component gap functions ($\Delta^{i.o.}_{xy-xz}$, $\Delta^{i.o.}_{xy-yz}$) and (Δ^{f}_{xz}, Δ^{f}_{yz}), we can form the linear combination $\Delta_{\mathrm{TRSI}} = \Delta_1 + \Delta_2$ (or equivalently $\Delta_1 - \Delta_2$) which preserves time-reversal symmetry invariance (TRSI). It transforms into itself under time reversal, up to a global sign (Table I). In contrast, $\Delta_{\mathrm{TRSB}} = \Delta_1 + i\Delta_2$ transforms into its complex conjugate and hence breaks time-reversal symmetry (TRSB). This is also the case of any linear combination $\Delta_1 + e^{i\varphi}\Delta_2$ with $\varphi \neq 0, \pi$.

The current experimental situation about time-reversal symmetry is not entirely clear. Kerr effect measurements [66], as well as μSR [62,65,67,68], suggest TRSB. In contrast, the expected spontaneous magnetization of a TRSB state could not be observed by scanning superconducting quantum interference device microscopy [69,70] or scanning Hall probes [71]. Additionally, recent Josephson tunneling measurements under an applied magnetic field suggest that time-reversal symmetry is preserved (TRSI) [72]. We therefore consider both possibilities in the following, corresponding to the two linear combinations above.

C. Gap zeros and lines of gapless quasiparticles

There is strong experimental evidence that Sr_2RuO_4 hosts gapless excitations, as indicated in particular by measurements of the specific heat [73–77], ultrasound attenuation [78], penetration depth [79], directional thermal conductivity [80], or Bogoliubov QPI [57]. Furthermore, thermal conductivity and QPI indicate that the gapless quasiparticles reside on lines in momentum space which run along the c axis, often referred to as "vertical line nodes." It is, however, often emphasized in this context that the indications for a two-component order parameter appear to be at odds with "vertical line nodes." Indeed, the most commonly discussed two-component order parameter has $d_{xz} \propto k_x k_z$, $d_{yz} \propto k_y k_z$ so that the modulus of the order parameter vanishes along "horizontal line nodes" (lying in planes perpendicular to the c axis). As shown below, we find, remarkably, that the interorbital singlet state reconciles a two-component order parameter with lines of gapless quasiparticles running along the c axis.

1. Momentum dependence of the gap

We first consider the momentum dependence of the gap function. In the previous sections, the gap function was expressed in the orbital basis as $\Delta_{ab}(\mathbf{k})$. Here, we instead consider it in the band basis $\nu \in \{\alpha, \beta, \gamma\}$, performing a basis change:

$$\Delta_{\mu\nu}(\mathbf{k}) = \sum_{ab} \langle \psi_{\mathbf{k}\mu} | \varphi_a \rangle \Delta_{ab}(\mathbf{k}) \langle \varphi_b | \psi_{\mathbf{k}\nu} \rangle, \tag{19}$$

where $\langle \psi_{\mathbf{k}\mu} | \varphi_a \rangle$ are the overlap matrix elements between the local orbital states $|\varphi_a\rangle$ with $a \in \{xy, xz, yz\}$ and the quasiparticle Bloch states $|\psi_{\mathbf{k}\mu}\rangle$. The interplay of hopping and SOC leads to a strongly mixed $\mathbf{k}$-dependent orbital character of $|\psi_{\mathbf{k}\mu}\rangle$ as can also be seen in Fig. 1, where the color code of the Fermi-surface sheet corresponds directly to the squared matrix elements $\langle \psi_{\mathbf{k}\mu} | \varphi_a \rangle^2$. It is important to note that a strong $\mathbf{k}$ dependence (angular dependence) can be inherited from the matrix elements entering Eq. (19), even when $\Delta_{ab}(\mathbf{k}) \approx \Delta_{ab}$ is approximately $\mathbf{k}$ independent in the orbital basis. This is indeed what happens in the case of the interorbital pairing.

We plot the normalized absolute value of the resulting gap function in Fig. 6 for TRSB and TRSI combinations of our two-component interorbital singlet [Figs. 6(a) and 6(b)] and the f-wave singlet [Figs. 6(c) and 6(d)] gaps. We combine color-map overlays on the normal-state Fermi surface together with line plots $\Delta(\phi)$ along the four Fermi-surface sheets found in the upper half plane of the first BZ for $k_z = 0$. The data in Fig. 6 show that generally linear combinations of the two gap components (i) break the C_4 symmetry along the z axis of the tetragonal normal-state model (due to this we distinguish in our plots between the α' and α sheets) and (ii) in the TRSB case break the Kramers degeneracy of the Cooper pair. For the TRSI gaps (orange), we have only one Kramers degenerate line while for the TRSB combinations (light and dark blue) we show the two split values of the gap (distinguished with superscripts $\Delta^{\mathrm{K1/K2}}$).

For the interorbital singlet gap function [see Figs. 6(a) and 6(b)] the first observation is its overall strong $\mathbf{k}$ dependence which originates almost entirely from the matrix elements $\langle \psi_{\mathbf{k}\mu} | \varphi_a \rangle$. The interorbital TRSI combination $\Delta^{i.o.}_{\mathrm{TRSI}} = \Delta^{i.o.}_{xy-xz} + \Delta^{i.o.}_{xy-yz}$ (orange) is finite on *all* Fermi-surface sheets. This is due to the SOC driven mixing of orbital character on the sheets. Indeed, the lowest absolute value of $\Delta^{i.o.}_{\mathrm{TRSI}}$ is found on the α' and α sheets (and specifically their intersection with the BZ diagonal) where the admixture of xy character is minimal (see Fig. 1).[2] Moreover, we observe a pronounced broken C_4 symmetry of $\Delta^{i.o.}_{\mathrm{TRSI}}$. For the specific TRSB combination $\Delta^{i.o.}_{\mathrm{TRSB}} = \Delta^{i.o.}_{xy-xz} + i\Delta^{i.o.}_{xy-yz}$ (light/dark blue) on the other hand, the C_4 symmetry is restored while Kramers degeneracy is broken $\Delta^{i.o\,\mathrm{K1}}_{\mathrm{TRSB}} \neq \Delta^{i.o\,\mathrm{K2}}_{\mathrm{TRSB}}$. We find an even more pronounced $\mathbf{k}$ dependence than for the TRSI case and, most remarkably, observe deep minima for $\Delta^{i.o.}_{\mathrm{TRSB}}$ particularly at the intersection of the α and β sheets with the BZ diagonal (marked by dashed black circles). Moreover, we note that there is a slight k_z dependence of the gap which originates from the change in orbital composition of the FS sheets [see dashed lines in Fig. 6(b)]. As can be seen from the plot, however, the deepest gap minima always remain on the α and β sheets parallel to the k_z axis which leads to one-dimensional lines of quasiparticle excitations perpendicular to the k_x/k_y plane ("vertical line nodes").

We now turn to the f-wave singlet for which we show data in Figs. 6(c) and 6(d). Here the pronounced $\mathbf{k}$ dependence of the gap in the orbital basis is entangled with that of the projection matrix elements. Also here we find the

[2]The finite value of xy character at the α sheets intersection originates from nonlocal hybridization of xz and yz orbitals. If this hybridization would be neglected, the xy character and indeed the value of the interorbital singlet gap would be zero at that point.

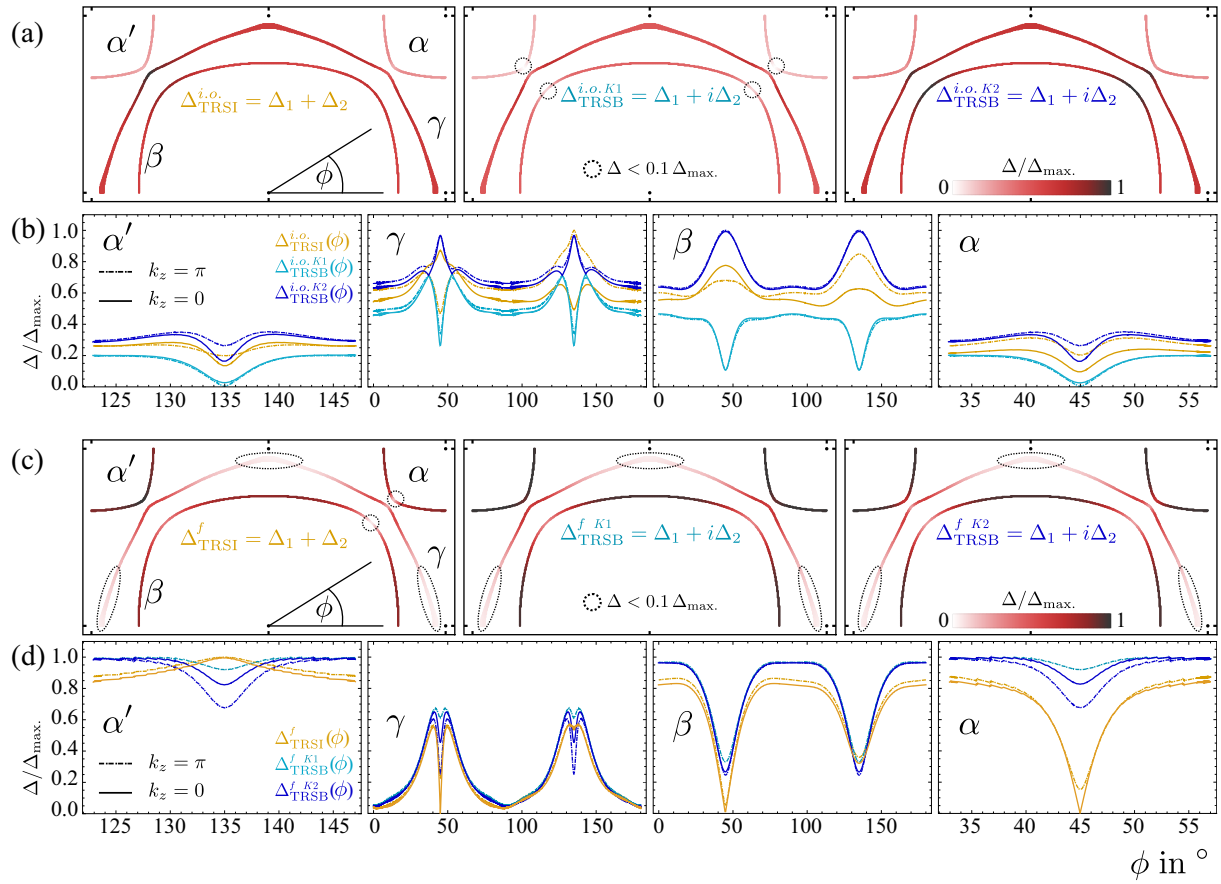

FIG. 6. Superconducting gap function in the eigenbasis of the quasiparticle bands at $\omega = 0$. (a) Color-map overlays on the normal-state Fermi surface of the interorbital gap function $\Delta^{i.o.}$, in the TRSI (left) and the Kramers-split TRSB (center and right) combinations. (b) Angular plots of $\Delta^{i.o.}$ along the four shown Fermi-surface sheets as a function of the angle Φ. (c) Same as (a) for Δ^{f}; (d) same as (b) for Δ^{f}. In (a) and (c) the dashed circles/ellipses indicate the location of the gap minima ($\Delta/\Delta_{\rm max} < 0.1$).

TRSI combination $\Delta^{f}_{\rm TRSI} = \Delta^{f}_{xz} + \Delta^{f}_{yz}$ (orange) to break the C_4 symmetry and the specific TRSB combination $\Delta^{f}_{\rm TRSB} = \Delta^{f}_{xz} + i\Delta^{f}_{\rm yz}$ (light/dark blue) to restore it. Different from the interorbital singlet, however, the deepest minima for the f-wave singlet occur (i) for the TRSI combination and (ii) most pronounced on the γ sheet where it cuts the k_x and k_y axes where the xy character is the strongest (which is not surprising given that this orbitally diagonal gap is weakest for the xy channel). Also, for the f-wave singlet gap the k_z dependence is not too strong [see dashed lines in Fig. 6(d)], so that also here one-dimensional quasiparticle lines along k_z occur.

2. *Gapless quasiparticles and momentum-resolved single-particle spectra*

In order to verify that the deep minima of the gap discussed in the previous section lead to quasiparticle excitations in the superconducting phase, we now compute the single-particle spectral function for a finite anomalous self-energy. As our results for the anomalous self-energy were performed above T_c, we estimate its overall amplitude to match experimental data for the specific heat. To this end, we computed the single-particle spectral function from the retarded normal propagator of the generalized Green's function (4):

$$A(\omega, \mathbf{k}) = -\lim_{\delta\to 0}\frac{1}{\pi}\mathrm{Im}[\mathrm{Tr}(\mathbf{G}(i\nu_n \to (\omega + i\delta), \mathbf{k}))]. \quad (20)$$

Using the $\mathbf{k}$-integrated spectral function $A(\omega)$ we then computed the specific heat via [81]

$$C_{\rm e}(T) = \int_0^\infty d\omega A(\omega)\frac{\omega^2}{k_{\rm B}T^2}\frac{1}{4\cosh^2(\omega/2k_{\rm B}T)}, \quad (21)$$

and found by comparison to experimental data [74] amplitudes of $\Delta_{\rm max} = 0.2/0.35$ meV for the interorbital and f-wave gap (see Appendix E). For this procedure we assumed (i) a temperature-independent anomalous self-energy and (ii) fitted its dependence on the fermionic Matsubara frequencies with an analytic model that allowed us to perform the analytic continuation as in Eq. (20). Details are reported in Appendix D.

Computation of $A(\omega, \mathbf{k})$ for small energies also allows us to plot the momentum-resolved residual spectral weight at $\omega = 0$ in the superconducting phase. The resulting plots for the TRSB combination of the interorbital pairing and the TRSB and TRSI combinations of the f-wave pairing are shown (at $k_z = 0$) in Fig. 7. In the plots (for which we have chosen a broadening factor in energy of $\delta = 10$ meV) we overlay the spectral weight (red color) on a gray background

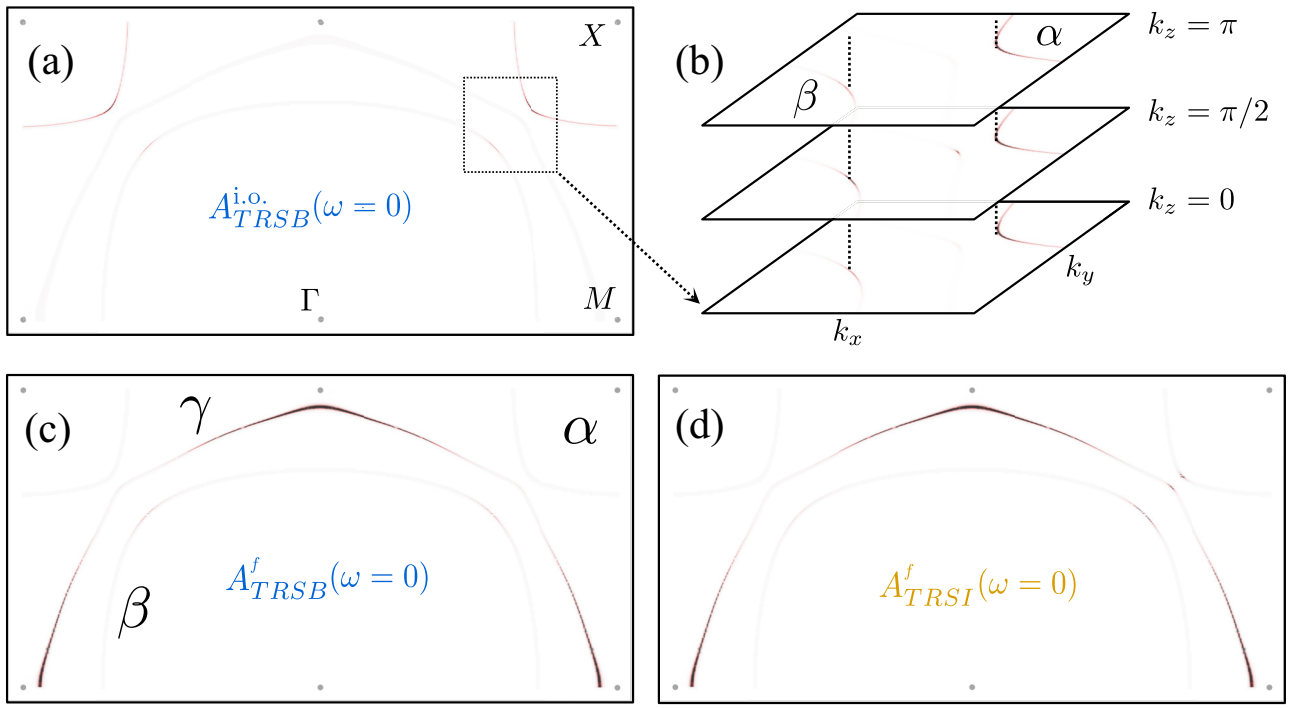

FIG. 7. Spectral weight at $\omega = 0$ calculated as Eq. (20) including normal and finite anomalous self-energies (i.e., gap functions). (a) $k_z = 0$ plane for finite interorbital singlet $\Delta^{i.o.}_{\text{TRSB}}$; (b) k_z dependence of the spectral weight for $\Delta^{i.o.}_{\text{TRSB}}$; (c) $k_z = 0$ plane for finite f-wave singlet Δ^{f}_{TRSB}; (d) $k_z = 0$ plane for finite f-wave singlet Δ^{f}_{TRSI}; as it is fully gapped, the TRSI combination of the interorbital singlet is omitted.

of the normal-state Fermi surface. Close inspection shows that the results are in agreement with our expectations from the plots of Δ in the band basis. As in the previous section, we start our discussion with the interorbital singlet pairing. The TRSI combination $(\Delta^{i.o.}_{xy-xz} + \Delta^{i.o.}_{xy-yz})$ (not shown on Fig. 7) leads to a fully gapped spectrum showing no residual spectral weight at the chosen energy resolution. The TRSB combination $(\Delta^{i.o.}_{xy-xz} + i\Delta^{i.o.}_{xy-yz})$, on the other hand, produces sizable weight in the regions of the gap minima on the α and β sheets (highlighted by dashed circles) located along the $|k_x| = |k_y|$ diagonals. Further, we point out an interesting effect for the interorbital pairing: the quasiparticle poles in the interorbital superconducting phase are not precisely found at the same momenta as the normal-state Fermi surface. Indeed, such momentum shifts of quasiparticles are generally expected for interorbital anomalous self-energies and were pointed out before [22]. In Appendix B we demonstrate this for a simple two-band model. We now turn to the f-wave singlet pairing. Also here we find the anticipated distribution of spectral weight. While there is some weight on the α and β sheets along the zone diagonal, most of the spectrum is found in the vicinity of the broad gap minima at the intersection of the γ pocket with the $k_x = 0$ and $k_y = 0$ lines.

The results we show in Fig. 7 can be directly compared to the symmetry analysis of Bogoliubov QPI experiments in [57]. This comparison likely rules out the f-wave singlet pairing as the experimentalists conclude for nodes and minima of the gap function in close vicinity of the normal state α and the β pockets along the diagonals. The only candidate which is in satisfactory agreement with this conclusion is the interorbital TRSB pairing $(\Delta^{i.o.}_{xy-xz} + i\Delta^{i.o.}_{xy-yz})$. We also point out that the Bogoliubov QPI experiments suggest an approximately fulfilled C_4 symmetry of the QPI pattern. It should be noted, though, that the slight deviations from full C_4 symmetry in favor of lower C_2 axes in the "unsymmetrized" raw data provided in the Supplemental Material of [57] could also be explained by a slight deviation from the perfect relative $\pi/2$ phase of the $\Delta^{i.o.}$ components in the TRSB combination.

VI. CONCLUSION

We have solved the linearized Eliashberg equation for Sr_2RuO_4 with a DMFT-based approximation at intermediate temperatures, and compared the leading symmetry channels of the superconducting order parameters to a large set of experiments. Our main candidate for the superconducting order is a two-component interorbital spin singlet with even spatial parity, and orbital antisymmetry. The time-reversal symmetry-breaking combination (TRSB) gap function has a strong angular dependence with deep minima along the Fermi-surface sheets and is compatible with the experiments, including one-dimensional lines of quasiparticles parallel to the c axis, located on the α and β sheets of the normal-state Fermi surface, on the zone diagonal. The driving force behind the interorbital singlet pairing appears to be local interorbital spin correlations. This indicates that Hund's coupling, which already dominates response functions in the normal state, remains key also for the superconducting pairing in Sr_2RuO_4. Finally, the interorbital order parameter is remarkably local when considered in the orbital basis. Therefore, it should be possible to obtain it directly within a multiorbital single-site DMFT study at low-temperature inside the superconducting

phase, which is certainly an interesting direction for future work.

ACKNOWLEDGMENTS

We acknowledge discussions with X. Cao, O. Gingras, and H. Menke. We acknowledge financial support by the Deutsche Forschungsgemeinschaft Project No. HA7277/3-1. The Flatiron Institute is a division of the Simons Foundation.

APPENDIX A: GENERALIZED PROPAGATORS

In the basis of the multiorbital Nambu spinor (3) the interacting generalized propagator reads as

$$\hat{\mathbf{G}}_{ab}(\mathbf{k},\tau) = -\langle \mathcal{T}_\tau \mathbf{\Psi}_a(\mathbf{k},\tau)\mathbf{\Psi}_b(\mathbf{k},0)^\dagger\rangle$$
$$= -\left\langle \mathcal{T}_\tau \begin{pmatrix} c_{a\uparrow}(\mathbf{k},\tau)c^\dagger_{b\uparrow}(\mathbf{k},0) & c_{a\uparrow}(\mathbf{k},\tau)c^\dagger_{b\downarrow}(\mathbf{k},0) & c_{a\uparrow}(\mathbf{k},\tau)c_{b\uparrow}(-\mathbf{k},0) & c_{a\uparrow}(\mathbf{k},\tau)c_{b\downarrow}(-\mathbf{k},0) \\ c_{a\downarrow}(\mathbf{k},\tau)c^\dagger_{b\uparrow}(\mathbf{k},0) & c_{a\downarrow}(\mathbf{k},\tau)c^\dagger_{b\downarrow}(\mathbf{k},0) & c_{a\downarrow}(\mathbf{k},\tau)c_{b\uparrow}(-\mathbf{k},0) & c_{a\downarrow}(\mathbf{k},\tau)c_{b\downarrow}(-\mathbf{k},0) \\ c^\dagger_{a\uparrow}(-\mathbf{k},\tau)c^\dagger_{b\uparrow}(\mathbf{k},0) & c^\dagger_{a\uparrow}(-\mathbf{k},\tau)c^\dagger_{b\downarrow}(\mathbf{k},0) & c^\dagger_{a\uparrow}(-\mathbf{k},\tau)c_{b\uparrow}(-\mathbf{k},0) & c^\dagger_{a\uparrow}(-\mathbf{k},\tau)c_{b\downarrow}(-\mathbf{k},0) \\ c^\dagger_{a\downarrow}(-\mathbf{k},\tau)c^\dagger_{b\uparrow}(\mathbf{k},0) & c^\dagger_{a\downarrow}(-\mathbf{k},\tau)c^\dagger_{b\downarrow}(\mathbf{k},0) & c^\dagger_{a\downarrow}(-\mathbf{k},\tau)c_{b\uparrow}(-\mathbf{k},0) & c^\dagger_{a\downarrow}(-\mathbf{k},\tau)c_{b\downarrow}(-\mathbf{k},0) \end{pmatrix} \right\rangle, \tag{A1}$$

with orbital indices a, b and time-ordering operator $\mathcal{T}_\tau$.

APPENDIX B: INTERORBITAL GAP FUNCTIONS

In order to illustrate how interorbital gap functions can shift spectral weight in momentum space at and around the Fermi energy ε_F, we consider this effect in the simplest possible model of two nonhybridized orbitals. We assume an interorbital singlet anomalous self-energy

$$\Delta^{\sigma\sigma'}_{ab} = \delta(\sigma-\sigma')\delta(1-|a-b|)\Delta, \tag{B1}$$

where $a,\ b \in \{1,2\}$ are orbital indices and $\sigma, \sigma' \in \{\uparrow,\downarrow\}$ are spin indices.

The generalized Green's function on the Nambu spinor basis (3) reads as

$$\hat{\mathbf{G}}(\mathbf{k}, i\omega_n)$$
$$= \begin{pmatrix} i\omega_n-\varepsilon^\uparrow_1(\mathbf{k}) & 0 & 0 & 0 & 0 & 0 & 0 & \Delta \\ 0 & i\omega_n-\varepsilon^\uparrow_2(\mathbf{k}) & 0 & 0 & 0 & 0 & -\Delta & 0 \\ 0 & 0 & i\omega_n-\varepsilon^\downarrow_1(\mathbf{k}) & 0 & 0 & \Delta & 0 & 0 \\ 0 & 0 & 0 & i\omega_n-\varepsilon^\downarrow_2(\mathbf{k}) & -\Delta & 0 & 0 & 0 \\ 0 & 0 & 0 & \Delta^* & i\omega_n+\varepsilon^\uparrow_1(\mathbf{k}) & 0 & 0 & 0 \\ 0 & 0 & -\Delta^* & 0 & 0 & i\omega_n+\varepsilon^\uparrow_2(\mathbf{k}) & 0 & 0 \\ 0 & \Delta^* & 0 & 0 & 0 & 0 & i\omega_n+\varepsilon^\downarrow_1(\mathbf{k}) & 0 \\ -\Delta^* & 0 & 0 & 0 & 0 & 0 & 0 & i\omega_n+\varepsilon^\downarrow_2(\mathbf{k}) \end{pmatrix}^{-1}, \tag{B2}$$

where $\varepsilon^\sigma_a(\mathbf{k})$ is the single-particle dispersion of orbital a with spin σ. We can solve Eq. (B2) and extract the spectral function (for finite Δ) as the trace of the imaginary part of the normal retarded Green's function

$$A(\omega,\mathbf{k}) = -\lim_{\delta\to 0}\frac{1}{\pi}\mathrm{Im}[\mathrm{Tr}(\mathbf{G}(i\nu_n\to(\omega+i\delta),\mathbf{k}))]. \tag{B3}$$

Assuming $\varepsilon^\uparrow_a(\mathbf{k}) = \varepsilon^\downarrow_a(\mathbf{k}) = \varepsilon_a(\mathbf{k})$, we find at $\omega = 0$ the expression

$$A(\omega=0,\mathbf{k}) = \left.\frac{2\delta[2\Delta^2+\varepsilon_1(\mathbf{k})^2+\varepsilon_2(\mathbf{k})^2)}{(\Delta^2+\varepsilon_1(\mathbf{k})\varepsilon_2(\mathbf{k})]^2}\right|_{\delta\to 0} \tag{B4}$$

which has poles along the contour

$$\Delta^2 = -\varepsilon_1(\mathbf{k})\varepsilon_2(\mathbf{k}). \tag{B5}$$

This is in stark contrast to an orbital diagonal gap which would be fully gapped:

$$\overline{A}(\omega=0,\mathbf{k}) = \delta\left(\frac{2}{\Delta^2_{\text{diag.}}+\varepsilon_1(\mathbf{k})^2}+\frac{2}{\Delta^2_{\text{diag.}}+\varepsilon_2(\mathbf{k})^2}\right)\Bigg|_{\delta\to 0}. \tag{B6}$$

From Eqs. (B4) and (B5) we see directly that even an interorbital $\mathbf{k}$-independent anomalous self-energy leads to a

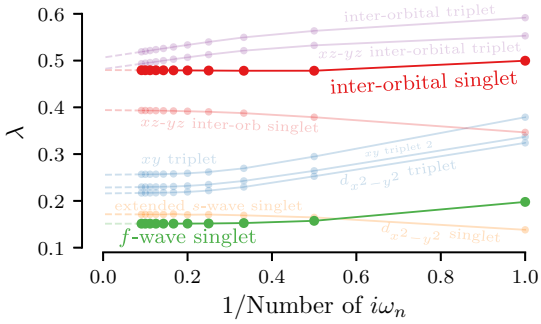

FIG. 8. Using more than one bosonic frequency for the DMFT vertex does not change the relative dominance for our gaps significantly and even makes the interorbital singlet more dominant.

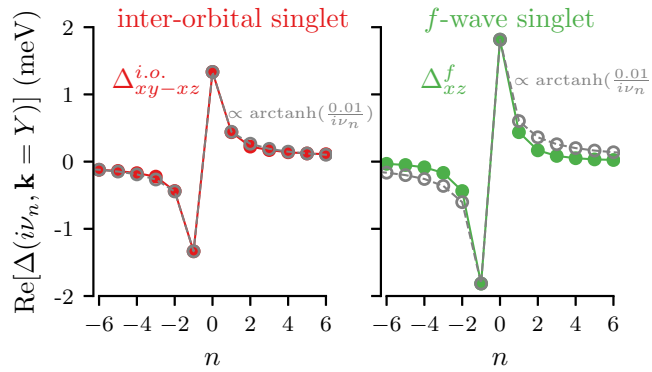

FIG. 9. The interorbital singlet and f-wave singlet show a frequency dependence which is in a reasonable agreement with the analytic dependence $\propto \mathrm{arctanh}(0.01/i\nu_n)$ behavior. These gaps stem from a calculation with a particle-particle vertex of 11 bosonic Matsubara frequencies.

k-dependent gap in the single-particle spectrum. Even more important is the realization that the quasiparticle poles that form the Bogoliubov Fermi surface in **k** space no longer coincide with the Fermi surfaces of the normal state (see also [82]). Different from an orbital diagonal pairing it is therefore *impossible* to extract the Bogoliubov Fermi surface by finding the intersections of the normal-state Fermi surface and the zeros of Δ.

Therefore, in order to address the topic of one-dimensional gapless nodal quasiparticles along "line nodes" (which are found roughly along k_z in Sr_2RuO_4) we always need to explicitly calculate the poles of the single-particle propagator. In our two-orbital toy model the contour (B5) still leads to two-dimensional Fermi-surface sheets in the three-dimensional BZ. In the three-orbital model, however, the interplay of spin-orbit coupling and interorbital Δ can lead to one-dimensional quasiparticle lines [22] as is the case for the interorbital prime candidate in Sr_2RuO_4 .

APPENDIX C: DEPENDENCE ON THE NUMBER OF BOSONIC MATSUBARA FREQUENCIES

To investigate if our results for the sampled two-particle Green's function $G^{(2)}$ are robust with respect to the number of considered bosonic Matsubara frequencies we calculate explicitly the dependencies of the Eliashberg eigenvalues λ from 1 up to 11 bosonic frequencies at $T \approx 386\,\mathrm{K}$ and then extrapolate to an infinite number of frequencies (see Fig. 8). The data show that (i) the λ values of our prime candidate gaps $\Delta^{i.o.}$ and Δ^{f} are well converged at the considered numbers of frequencies and (ii) that no other gap function trends strongly towards higher values. If these trends do not change to strongly with temperature, our conclusions should be insensitive to increasing the number of bosonic Matsubara frequencies further.

APPENDIX D: DEPENDENCE OF THE GAPS ON FERMIONIC MATSUBARA FREQUENCIES

From the calculation with 11 bosonic frequencies (Appendix C) we also get insight in the fermionic frequency dependence of our gap candidates (see Fig. 9). For a calculation with one bosonic frequency the gaps $\Delta(i\nu_n)$ are only nonzero at $i\nu_{n=-1,0}$; however, by increasing the number of bosonic frequencies they become nonzero at higher $i\nu_n$. By using 11 bosonic frequencies they show a converging behavior in reasonable agreement with the analytic frequency dependence $\propto \mathrm{arctanh}(0.01/i\nu_n)$.

To motivate this analytic frequency dependence we assume that $\Delta(i\nu_n)$ is analytical and converges for $|i\nu_n| \to \infty$, which allows us to use the spectral representation

$$\Delta(i\nu_n) = \int_{-\infty}^{\infty} d\omega \frac{A_\Delta(\omega)}{i\nu_n - \omega}. \tag{D1}$$

We consider an imaginary even box-shaped spectral function

$$A_\Delta(\omega) = i[\Theta(\omega + a) - \Theta(\omega - a)], \tag{D2}$$

where $2a$ is the box size. This yields

$$\Delta(i\nu_n) = \int_{-a}^{a} d\omega \frac{i}{i\nu_n - \omega} = 2i\,\mathrm{arctanh}\left(\frac{a}{i\nu_n}\right), \tag{D3}$$

which is odd in $i\nu_n$ and purely real. Using Eq. (D3) with $a = 0.01$ shows a reasonable agreement with the numerical data (see Fig. 9) supporting the chosen spectral function.

Note that by analytical continuing $i\nu_n \to \omega + i\delta$ [Eq. (D3)], as we do in Sec. V C 2, we get real frequency gaps $\Delta(\omega)$, which have a finite constant real part and a linear imaginary part. Therefore, these gaps do not vanish at $\omega = 0$ eV and gap the Fermi surface. This is different to other odd Matsubara frequency gaps, e.g., a linear behavior $\propto i\nu_n$, which leaves the Fermi surface ungapped [46,48].

APPENDIX E: FITTING GAP SIZE TO SPECIFIC HEAT

In order to estimate realistic overall prefactors of our gap function for the computation of spectral functions, we computed the low-temperature specific heat (21) and compared to experimental data [74].

For comparison, which is shown in Fig. 10, the spectral function was calculated for a $300 \times 300 \times 300$ **k** mesh and for 200 ω points from 0 to 1 meV. The integral (21) was solved numerically with SCIPY [83].

We calculated the electronic specific heat for multiple gap sizes $\Delta_{\max}$ of the analytic models to find the best fit to

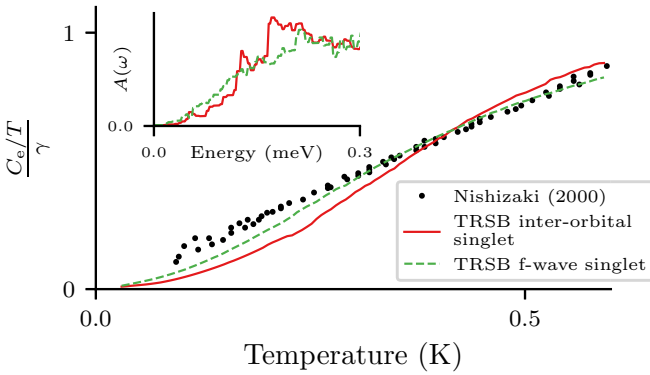

FIG. 10. Comparison of experimental data [74] and calculated temperature dependence of the specific heat for the interorbital singlet and f-wave gap (shown here in TRSB combination). The inset shows the **k**-integrated spectral function up to 0.3 meV.

the experimental data [74]. The best overall agreement was found for $\Delta_{\max} = 0.2$ meV for the interorbital and $\Delta_{\max} = 0.35$ meV for the f-wave singlet.

APPENDIX F: TWO-PARTICLE GREEN'S FUNCTION SAMPLING

We sample both the single-particle G_{ab} and two-particle $G^{(2)}_{abcd}$ Green's functions using CT-HYB and hybridization function removal [42]. The tetragonal symmetry of Sr_2RuO_4 causes the single-particle Green's function to be diagonal in the t_{2g} Wannier orbital space $G_{ab} = \delta_{ab} G_{aa}$. This symmetry is due to the DMFT self-consistency shared with the impurity hybridization function $\widetilde{\Delta}_{ab} = \delta_{ab}\widetilde{\Delta}_{aa}$. Hence, all nonzero components of G_{ab} can be sampled by removal of hybridization insertions in the expansion of the partition function. This is, unfortunately, not the case for the two-particle Green's function $G^{(2)}_{abcd}$. The spin-flip and pair-hopping terms in the local Kanamori interaction generate nonzero orbital combinations *abcd* that can not be sampled when the hybridization function is diagonal in orbital space. Hence, in order to measure all components of $G^{(2)}_{abcd}$, we perform a single-particle basis transform of the impurity model to a basis were all *ab* components of $\widetilde{\Delta}_{ab}$ are nonzero. However, an off-diagonal $\widetilde{\Delta}$ generates a Monte Carlo sign problem, making low-temperature calculations unfeasible [14]. For this study we had to restrict ourselves to temperatures $T \gtrsim 290$ K.

APPENDIX G: STATIC APPROXIMATION OF THE FULLY IRREDUCIBLE VERTEX FUNCTION

In our calculations we approximate the fully irreducible vertex $\Lambda^{s/t}$ with the static first-order term $\widetilde{\Lambda}^{s/t}$, neglecting fourth-order corrections $\Lambda^{s/t} \approx \widetilde{\Lambda}^{s/t}$. The first order fully irreducible vertex $\widetilde{\Lambda}^{s/t}$ is given by

$$\widetilde{\Lambda}^{\mathrm{s}} \equiv -\tfrac{1}{2}U^d - \tfrac{3}{2}U^m, \tag{G1}$$

$$\widetilde{\Lambda}^{\mathrm{t}} \equiv -\tfrac{1}{2}U^d + \tfrac{1}{2}U^m, \tag{G2}$$

where $U^{d/m}$ are the static interaction tensors of the rotationally invariant Kanamori interaction

$$U^d_{abcd} = \begin{cases} U, & \text{if } a=b=c=d \\ -U'+2J, & \text{if } a=d\neq b=c \\ 2U'-J, & \text{if } a=b\neq c=d \\ J, & \text{if } a=c\neq b=d \\ 0, & \text{else} \end{cases} \tag{G3}$$

$$U^m_{abcd} = \begin{cases} U, & \text{if } a=b=c=d \\ U', & \text{if } a=d\neq b=c \\ J, & \text{if } a=b\neq c=d \\ J, & \text{if } a=c\neq b=d \\ 0, & \text{else} \end{cases} \tag{G4}$$

with $U' = U - 2J$, and use the same values for the Hubbard interaction U and the Hund's J as in our self-consistent DMFT calculations $U = 2.3$ eV, $J = 0.4$ eV.

APPENDIX H: STATIC APPROXIMATION OF Γ IN THE EQUATION FOR THE VERTEX LADDER

Conceptually, the ladder vertex $\Phi^{d/m}$ [Eq. (13)] can be approximated using the DMFT impurity vertex $\Gamma^{d/m}_{\mathrm{DMFT}}$ and the DMFT generalized lattice susceptibility $\chi^{d/m}_{\mathrm{DMFT}}$ obtained from the Bethe-Salpeter equation [see Eq. (14)]

$$\Phi^{d/m}[\Gamma^{d/m}, \chi^{d/m}] \approx \Phi^{d/m}\big[\Gamma^{d/m}_{\mathrm{DMFT}}, \chi^{d/m}_{\mathrm{DMFT}}\big] \equiv \Phi^{d/m}_{\mathrm{DMFT}}. \tag{H1}$$

However, $\Phi^{d/m}_{\mathrm{DMFT}}$ can not be used in the Parquet equation, due to stochastic quantum Monte Carlo noise at higher frequencies, introduced through $\Gamma^{d/m}_{\mathrm{DMFT}}$. Therefore, we resort to the renormalized static approximation $\Gamma^{d/m}_{\mathrm{DMFT}} \approx \overline{U}^{d/m}$, which leads to

$$\begin{aligned} \Phi^{d/m}[\Gamma^{d/m}, \chi^{d/m}] &\approx \Phi^{d/m}\big[\overline{U}^{d/m}, \chi^{d/m}_{\mathrm{DMFT}}\big] \\ &= \overline{U}^{d/m}\chi^{d/m}_{\mathrm{DMFT}}(i\omega_n, \mathbf{q})\,\overline{U}^{d/m} \\ &\equiv \widetilde{\Phi}^{d/m}(i\omega_n, \mathbf{q}), \end{aligned} \tag{H2}$$

where $\overline{U}^{d/m}$ are static renormalized interaction tensors.

Finally, we obtain an approximation for the exact particle-particle vertex $\Gamma^{s/t}$ [Eqs. (12) and (11)] by combining the two static approximations $\Lambda \approx \widetilde{\Lambda}$ [Eq. (G1)] and $\Phi \approx \widetilde{\Phi}$ [Eq. (H2)]:

$$\Gamma^{s/t}[\Lambda^{s/t}, \Phi^{d/m}] \approx \Gamma^{s/t}[\widetilde{\Lambda}^{s/t}, \widetilde{\Phi}^{d/m}] \equiv \widetilde{\Gamma}^{s/t}. \tag{H3}$$

The (orbital-dependent) renormalized interaction tensors $\overline{U}^{d/m}$ were obtained by minimizing

$$\min_{\overline{U}^{d/m}} \sum_{\mathbf{q}} \Big|\Gamma^{s/t}\big[\widetilde{\Lambda}^{s/t}, \Phi^{d/m}_{\mathrm{DMFT}}\big] - \widetilde{\Gamma}^{s/t}\Big|^2 \tag{H4}$$

in the low-frequency limit, i.e., for the zeroth bosonic Matsubara frequency $\omega_0 = 0$ and first fermionic Matsubara frequencies $\nu_0 = \nu'_0 = \pi/\beta$. In Fig. 11 we show the

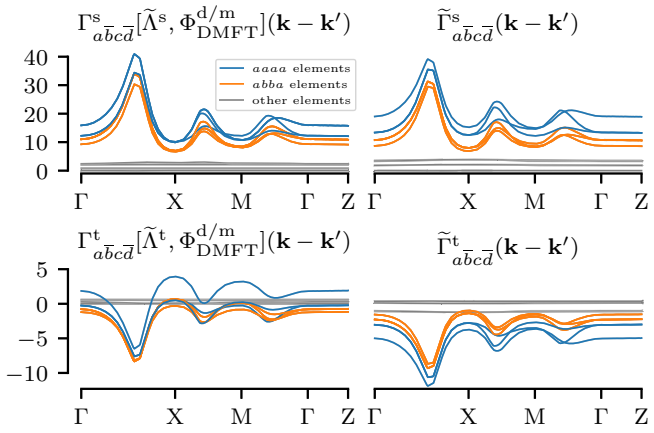

FIG. 11. The singlet vertex at the zeroth bosonic Matsubara frequency $\omega_0 = 0$ and first fermionic Matsubara frequencies $\nu_0 = \nu_0' = \pi/\beta$ (top left) is well matched by our static interaction approximation (top right), while the triplet vertices differ visibly (bottom).

comparison for $\overline{U}_{xy} = 1.2$ eV and $\overline{U}_{xz/yz} = 1.1$ eV. The exact structure of $\overline{U}^{d/m}$ is given by

$$\overline{U}^{d}_{abcd} = \begin{cases} \overline{U}_{xy}, & \text{if } a=b=c=d=xy \\ \overline{U}_{xz/yz}, & \text{if } a=b=c=d=xz/yz \\ -\overline{U}' + 2\overline{J}, & \text{if } a=d\neq b=c \\ 2\overline{U}' - \overline{J}, & \text{if } a=b\neq c=d \\ \overline{J}, & \text{if } a=c\neq b=d \\ 0, & \text{else} \end{cases} \tag{H5}$$

$$\overline{U}^{m}_{abcd} = \begin{cases} \overline{U}_{xy}, & \text{if } a=b=c=d=xy \\ \overline{U}_{xz/yz}, & \text{if } a=b=c=d=xz/yz \\ \overline{U}', & \text{if } a=d\neq b=c \\ \overline{J}, & \text{if } a=b\neq c=d \\ \overline{J}, & \text{if } a=c\neq b=d \\ 0, & \text{else.} \end{cases} \tag{H6}$$

Here $\overline{U}_{xy}$ and $\overline{U}_{xz/yz}$ are the free parameters, while the others are constrained by $\overline{J}/\overline{U}_{\mathrm{avg}} = 0.4/2.3$ and $\overline{U}' = \overline{U}_{\mathrm{avg}} - 2\overline{J}$ with $\overline{U}_{\mathrm{avg}} = \frac{1}{3}(\overline{U}_{xy} + 2\overline{U}_{xz/yz})$.

APPENDIX I: NUMERICAL DETAILS

We sample the one- and two-particle Green's function with the CT-HYB solver implemented in the TRIQS project [84,85]. We use a $32 \times 32 \times 32$ k mesh and do 10^9 (2.1×10^8) Monte Carlo cycles for the one- (two-) particle Green's function. For sampling the two-particle Green's function $G^{(2)}$ we employ the particle-hole notation using a 40×40 fermionic frequency grid and only one bosonic frequency. To investigate if the restriction of using only one bosonic frequency is critical for our results, we additionally sample $G^{(2)}$ for 11 bosonic frequencies at $T \approx 386$ K (cf. Appendix C).

We solve the impurity and lattice Bethe-Salpeter equations to obtain $\Gamma^{d/m}/\chi^{d/m}$ [14] with the two-particle response function toolbox (TPRF) of the TRIQS library [86]. Both the impurity and lattice Bethe-Salpeter equations are matrix equations in (fermionic) Matsubara space, which we solve using three finite-frequency cutoffs $n_\nu = 20, 30, 40$ from which we then extrapolated $\chi^{d/m}$ to infinite frequencies.

The linearized Eliashberg equation (8) is technically a large eigenvalue problem in a vector space spanned by the orbital, frequency, and momentum indices. To find (generally complex) eigenvectors Δ and their corresponding eigenvalues λ we employ TPRF [86]. In TPRF the implicit matrix-vector product $(\Gamma GG) \cdot \Delta$ is implemented using fast Fourier transforms, and the highest eigenvalues λ and eigenvectors Δ are determined using the implicitly restarted Arnoldi method from the ARPACK library [87] through the SCIPY package [83]. The Pauli principle [i.e., the *SPOT* condition (18)] is exploited to constrain the solutions to all possible allowed symmetries, further reducing the computational effort. No other restrictions are imposed on Δ.

APPENDIX J: SCALING $\chi^{d/m}$ FOR CHANNEL ANALYSIS

We distinguish between magnetic, density, interorbital and intraorbital, and local fluctuations in our channel analysis by scaling selected components of $\chi^{d/m}$ before they enter the equation for the pairing vertices (11) and (12) via the reducible vertex function (13). To study the effect of magnetic (density) fluctuations we scale the complete χ^m (χ^d) tensor. For the intraorbital fluctuations we solely scale the components of the density and magnetic susceptibility where all indices are equal, i.e., only the $\chi^{d/m}_{aaaa}$ components. Complementary, for the interorbital fluctuations we scale all

TABLE II. The first five leading gaps in descending order in RPA at $T \approx 290$ K, $U = 0.575$ eV, and $J = 0.1$ eV (cf. Fig. 12). Gaps with the same *SPOT* symmetry share the same color. As many of our gap functions have not only a single finite matrix element in the orbital space the column "Orbital character" indicates the dominant orbital matrix element.

	Symmetries				
Pairing	Spin	Parity	Orbital	Time	Orbital character
$d_{x^2-y^2}$ singlet	−	+	+	+	intra xy
Interorbital triplet	+	+	−	+	degenerate { inter xy-yz / interxy-xz
xy triplet	+	+	+	−	intra xy
xz-yz interorbital triplet	+	+	−	+	inter xz-yz
Interorbital singlet	−	+	−	−	degenerate { inter xy-yz / interxy-xz

components except for the $\chi^{d/m}_{aaaa}$ components. For studying local fluctuations we first calculate the local susceptibilities via

$$\chi^{d/m}_{\mathrm{loc}} = \frac{1}{N_{\mathbf{k}}} \sum_{\mathrm{BZ}} \chi^{d/m}(\mathbf{k}), \tag{J1}$$

which allows us to express the susceptibilities as a sum of $\chi^{d/m}_{\mathrm{loc}}$ and a dispersive part, i.e.,

$$\chi^{d/m}(\mathbf{k}) = \chi^{d/m}_{\mathrm{local}} + \chi^{d/m}_{\mathrm{dispersive}}(\mathbf{k}). \tag{J2}$$

We then only scale $\chi^{d/m}_{\mathrm{loc}}$ for the channel analysis.

APPENDIX K: RANDOM PHASE APPROXIMATION

As a benchmark we solve the linearized Eliashberg equation in the random phase approximation (RPA). In RPA the interaction is only treated on the level of the two-particle Green's function, hence, we use the spin-independent noninteracting Green's function

$$G^0_{ab}(\nu_n, \mathbf{k}) = [(i\nu_n + \mu)\mathbf{1} - \epsilon_{\mathbf{k}}]^{-1}_{ab}, \tag{K1}$$

where μ is the chemical potential and $\epsilon_{\mathbf{k}}$ the dispersion relation, instead of G inside Eq. (8). To construct the particle-particle vertices in RPA we use the equations introduced in Appendixes G and H, but use the RPA density and magnetic susceptibilities given by

$$\chi^{d/m,\mathrm{RPA}}_{abcd}(Q) = \frac{\chi^{0,d/m}(Q)}{1 \pm U^{d/m}\chi^{0,d/m}(Q)}, \tag{K2}$$

with the bare susceptibility

$$\chi^{0,d/m}_{abcd}(Q) = -\frac{1}{N_{\mathbf{k}}\beta} \sum_{K} G^0_{bc}(K) G^0_{da}(K+Q), \tag{K3}$$

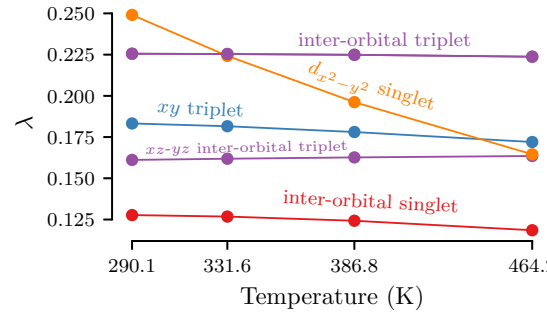

FIG. 12. The $d_{x^2-y^2}$ singlet gap takes the lead for lower temperatures in RPA. The doubly degenerate interorbital singlet, which is the dominant one in DMFT, remains low tier.

and the local vertex $U^{d/m}$ given in Eq. (G4). We use the renormalized interaction parameters $U = 0.575$ eV and $J = 0.1$ eV, which have the same U/J ratio as the DMFT parameters but are smaller, because otherwise the RPA susceptibilities diverge.

We identify the following leading superconducting gap functions: a $d_{x^2-y^2}$ singlet, a doubly degenerate interorbital triplet that couples xy with xz/yz, an odd-frequency triplet, an interorbital triplet that couples xz with yz, and the doubly degenerate interorbital singlet that couples xy with xz/yz (see Table II). Their eigenvalues over temperature are pictured in Fig. 12.

While the doubly degenerate interorbital triplet leads for the higher temperatures, the $d_{x^2-y^2}$ singlet rapidly increases for lower temperatures where it becomes dominant. This result is in agreement with other RPA studies [43,44], but also with RPA like schemes that try to capture correlation effects by dressing the noninteracting Green's function [25]. The doubly degenerate interorbital singlet, which is dominant in our DMFT calculation, is also present among the leading gaps, but remains low tier.

[1] Y. Maeno, H. Hashimoto, K. Yoshida, S. Nishizaki, T. Fujita, J. G. Bednorz, and F. Lichtenberg, Superconductivity in a layered perovskite without copper, Nature (London) **372**, 532 (1994).

[2] C. Bergemann, A. P. Mackenzie, S. R. Julian, D. Forsythe, and E. Ohmichi, Quasi-two-dimensional Fermi liquid properties of the unconventional superconductor Sr_2RuO_4, Adv. Phys. **52**, 639 (2003).

[3] A. P. Mackenzie and Y. Maeno, The superconductivity of Sr_2RuO_4 and the physics of spin-triplet pairing, Rev. Mod. Phys. **75**, 657 (2003).

[4] A. Pustogow, Y. Luo, A. Chronister, Y. S. Su, D. A. Sokolov, F. Jerzembeck, A. P. Mackenzie, C. W. Hicks, N. Kikugawa, S. Raghu, E. D. Bauer, and S. E. Brown, Constraints on the superconducting order parameter in Sr_2RuO_4 from oxygen-17 nuclear magnetic resonance, Nature (London) **574**, 72 (2019).

[5] K. Ishida, M. Manago, K. Kinjo, and Y. Maeno, Reduction of the ^{17}O knight shift in the superconducting state and the heat-up effect by NMR pulses on Sr_2RuO_4, J. Phys. Soc. Jpn. **89**, 034712 (2020).

[6] A. P. Mackenzie, A Personal Perspective on the Unconventional Superconductivity of Sr_2RuO_4, J. Supercond. Novel Magn. **33**, 177 (2020).

[7] A. P. Mackenzie, T. Scaffidi, C. W. Hicks, and Y. Maeno, Even odder after twenty-three years: The superconducting order parameter puzzle of Sr_2RuO_4, npj Quantum Mater. **2**, 40 (2017).

[8] S. A. Kivelson, A. C. Yuan, B. Ramshaw, and R. Thomale, A proposal for reconciling diverse experiments on the superconducting state in Sr_2RuO_4, npj Quantum Mater. **5**, 43 (2020).

[9] A. Georges, G. Kotliar, W. Krauth, and M. J. Rozenberg, Dynamical mean-field theory of strongly correlated fermion systems and the limit of infinite dimensions, Rev. Mod. Phys. **68**, 13 (1996).

[10] G. Kotliar, S. Y. Savrasov, K. Haule, V. S. Oudovenko, O. Parcollet, and C. A. Marianetti, Electronic structure calculations with dynamical mean-field theory, Rev. Mod. Phys. **78**, 865 (2006).

[11] J. Mravlje, M. Aichhorn, T. Miyake, K. Haule, G. Kotliar, and A. Georges, Coherence-Incoherence Crossover and the

Mass-Renormalization Puzzles in Sr_2RuO_4, Phys. Rev. Lett. **106**, 096401 (2011).

[12] A. Tamai, M. Zingl, E. Rozbicki, E. Cappelli, S. Riccò, A. de la Torre, S. McKeown Walker, F. Y. Bruno, P. D. C. King, W. Meevasana, M. Shi, M. Radović, N. C. Plumb, A. S. Gibbs, A. P. Mackenzie, C. Berthod, H. U. R. Strand, M. Kim, A. Georges, and F. Baumberger, High-Resolution Photoemission on Sr_2RuO_4 Reveals Correlation-Enhanced Effective Spin-Orbit Coupling and Dominantly Local Self-Energies, Phys. Rev. X **9**, 021048 (2019).

[13] L. Boehnke, P. Werner, and F. Lechermann, Multi-orbital nature of the spin fluctuations in Sr_2RuO_4, Europhys. Lett. **122**, 57001 (2018).

[14] H. U. R. Strand, M. Zingl, N. Wentzell, O. Parcollet, and A. Georges, Magnetic response of Sr_2RuO_4: Quasi-local spin fluctuations due to Hund's coupling, Phys. Rev. B **100**, 125120 (2019).

[15] S. Acharya, D. Pashov, C. Weber, H. Park, L. Sponza, and M. V. Schilfgaarde, Evening out the spin and charge parity to increase T_c in Sr_2RuO_4, Commun. Phys. **2**, 163 (2019).

[16] P. Steffens, Y. Sidis, J. Kulda, Z. Q. Mao, Y. Maeno, I. I. Mazin, and M. Braden, Spin Fluctuations in Sr_2RuO_4 from Polarized Neutron Scattering: Implications for Superconductivity, Phys. Rev. Lett. **122**, 047004 (2019).

[17] A. Georges, L. d. Medici, and J. Mravlje, Strong correlations from hund's coupling, Annu. Rev. Condens. Matter Phys. **4**, 137 (2013).

[18] K. Haule and G. Kotliar, Coherence-incoherence crossover in the normal state of iron oxypnictides and importance of Hund's rule coupling, New J. Phys. **11**, 025021 (2009).

[19] P. Hansmann, R. Arita, A. Toschi, S. Sakai, G. Sangiovanni, and K. Held, Dichotomy between Large Local and Small Ordered Magnetic Moments in Iron-Based Superconductors, Phys. Rev. Lett. **104**, 197002 (2010).

[20] Z. P. Yin, K. Haule, and G. Kotliar, Kinetic frustration and the nature of the magnetic and paramagnetic states in iron pnictides and iron chalcogenides, Nat. Mater. **10**, 932 (2011).

[21] A. Toschi, R. Arita, P. Hansmann, G. Sangiovanni, and K. Held, Quantum dynamical screening of the local magnetic moment in Fe-based superconductors, Phys. Rev. B **86**, 064411 (2012).

[22] S.-O. Kaba and D. Sénéchal, Group-theoretical classification of superconducting states of strontium ruthenate, Phys. Rev. B **100**, 214507 (2019).

[23] A. Ramires and M. Sigrist, Identifying detrimental effects for multiorbital superconductivity: Application to Sr_2RuO_4, Phys. Rev. B **94**, 104501 (2016).

[24] A. Ramires and M. Sigrist, Superconducting order parameter of Sr_2RuO_4: A microscopic perspective, Phys. Rev. B **100**, 104501 (2019).

[25] O. Gingras, R. Nourafkan, A.-M. S. Tremblay, and M. Côté, Superconducting Symmetries of Sr_2RuO_4 from First-Principles Electronic Structure, Phys. Rev. Lett. **123**, 217005 (2019).

[26] M. W. Haverkort, I. S. Elfimov, L. H. Tjeng, G. A. Sawatzky, and A. Damascelli, Strong Spin-Orbit Coupling Effects on the Fermi Surface of Sr_2RuO_4 and Sr_2RhO_4, Phys. Rev. Lett. **101**, 026406 (2008).

[27] C. N. Veenstra, Z.-H. Zhu, M. Raichle, B. M. Ludbrook, A. Nicolaou, B. Slomski, G. Landolt, S. Kittaka, Y. Maeno, J. H. Dil, I. S. Elfimov, M. W. Haverkort, and A. Damascelli, Spin-Orbital Entanglement and the Breakdown of Singlets and Triplets in Sr_2RuO_4 Revealed by Spin- and Angle-Resolved Photoemission Spectroscopy, Phys. Rev. Lett. **112**, 127002 (2014).

[28] G. Zhang, E. Gorelov, E. Sarvestani, and E. Pavarini, Fermi Surface of Sr_2RuO_4: Spin-Orbit and Anisotropic Coulomb Interaction Effects, Phys. Rev. Lett. **116**, 106402 (2016).

[29] M. Kim, J. Mravlje, M. Ferrero, O. Parcollet, and A. Georges, Spin-Orbit Coupling and Electronic Correlations in Sr_2RuO_4, Phys. Rev. Lett. **120**, 126401 (2018).

[30] P. Blaha, K. Schwarz, G. K. H. Madsen, D. Kvasnicka, J. Luitz, R. Laskowski, F. Tran, and L. D. Marks, *WIEN2k: An Augmented Plane Wave plus Local Orbitals Program for Calculating Crystal Properties* (Karlheinz Schwarz, Techn. Universität Wien, Austria, 2018).

[31] J. Kuneš, R. Arita, P. Wissgott, A. Toschi, H. Ikeda, and K. Held, Wien2wannier: From linearized augmented plane waves to maximally localized Wannier functions, Comput. Phys. Commun. **181**, 1888 (2010); N. Marzari and D. Vanderbilt, Maximally localized generalized Wannier functions for composite energy bands, Phys. Rev. B **56**, 12847 (1997); A. A. Mostofi, J. R. Yates, Y. S. Lee, I. Souza, D. Vanderbilt, and N. Marzari, wannier90: A tool for obtaining maximally-localised Wannier functions, Comput. Phys. Commun. **178**, 685 (2008); N. Marzari, A. A. Mostofi, J. R. Yates, I. Souza, and D. Vanderbilt, Maximally localized Wannier functions: Theory and applications, Rev. Mod. Phys. **84**, 1419 (2012).

[32] E. Gull, O. Parcollet, and A. J. Millis, Superconductivity and the Pseudogap in the Two-Dimensional Hubbard Model, Phys. Rev. Lett. **110**, 216405 (2013).

[33] G. M. Eliashberg, Interactions between electrons and lattice vibrations in a superconductor, J. Exptl. Theoret. Phys. (U.S.S.R.) **38**, 966 (1960) [J. Exp. Theor. Phys. **11**, 696 (1960)].

[34] A. A. Abrikosov, I. Dzyaloshinskii, L. P. Gorkov, and R. A. Silverman, *Methods of Quantum Field Theory in Statistical Physics* (Dover, New York, 1975).

[35] R. Nourafkan, G. Kotliar, and A.-M. S. Tremblay, Correlation-Enhanced Odd-Parity Interorbital Singlet Pairing in the Iron-Pnictide Superconductor LiFeAs, Phys. Rev. Lett. **117**, 137001 (2016).

[36] N. E. Bickers, Self-Consistent Many-Body Theory for Condensed Matter Systems, in *Theoretical Methods for Strongly Correlated Electrons*, edited by D. Sénéchal, A. M. Tremblay, and C. Bourbonnais, CRM Series in Mathematical Physics (Springer, New York, 2004), pp. 237–296.

[37] G. Rohringer, New routes towards a theoretical treatment of nonlocal electronic correlations, Ph.D. thesis, Technischen Universität Wien, 2013.

[38] G. Rohringer, H. Hafermann, A. Toschi, A. A. Katanin, A. E. Antipov, M. I. Katsnelson, A. I. Lichtenstein, A. N. Rubtsov, and K. Held, Diagrammatic routes to nonlocal correlations beyond dynamical mean field theory, Rev. Mod. Phys. **90**, 025003 (2018).

[39] P. Werner and A. J. Millis, Hybridization expansion impurity solver: General formulation and application to Kondo lattice and two-orbital models, Phys. Rev. B **74**, 155107 (2006).

[40] P. Werner, A. Comanac, L. de Medici, M. Troyer, and A. J. Millis, Continuous-Time Solver for Quantum Impurity Models, Phys. Rev. Lett. **97**, 076405 (2006).

[41] K. Haule, Quantum Monte Carlo impurity solver for cluster dynamical mean-field theory and electronic structure calculations with adjustable cluster base, Phys. Rev. B **75**, 155113 (2007).

[42] E. Gull, A. J. Millis, A. I. Lichtenstein, A. N. Rubtsov, M. Troyer, and P. Werner, Continuous-time Monte Carlo methods for quantum impurity models, Rev. Mod. Phys. **83**, 349 (2011).

[43] L.-D. Zhang, W. Huang, F. Yang, and H. Yao, Superconducting pairing in Sr_2RuO_4 from weak to intermediate coupling, Phys. Rev. B **97**, 060510(R) (2018).

[44] A. T. Rømer, D. D. Scherer, I. M. Eremin, P. J. Hirschfeld, and B. M. Andersen, Knight Shift and Leading Superconducting Instability from Spin Fluctuations in Sr_2RuO_4, Phys. Rev. Lett. **123**, 247001 (2019).

[45] T. Scaffidi, J. C. Romers, and S. H. Simon, Pairing symmetry and dominant band in Sr_2RuO_4, Phys. Rev. B **89**, 220510(R) (2014).

[46] J. Linder and A. V. Balatsky, Odd-frequency superconductivity, Rev. Mod. Phys. **91**, 045005 (2019).

[47] V. Berezinskiç, New model of the anisotropic phase of superfluid He^3, Zh. Eksp. Teor. Fiz. Pis'ma Red. **20**, 628 (1974) [Sov. J. Exper. Theor. Phys. Lett. **20**, 287 (1974)].

[48] A. Balatsky and E. Abrahams, New class of singlet superconductors which break the time reversal and parity, Phys. Rev. B **45**, 13125(R) (1992).

[49] R. Heid, On the thermodynamic stability of odd-frequency superconductors, Z. Phys. B **99**, 15 (1995).

[50] D. Solenov, I. Martin, and D. Mozyrsky, Thermodynamical stability of odd-frequency superconducting state, Phys. Rev. B **79**, 132502 (2009).

[51] Y. V. Fominov, Y. Tanaka, Y. Asano, and M. Eschrig, Odd-frequency superconducting states with different types of Meissner response: Problem of coexistence, Phys. Rev. B **91**, 144514 (2015).

[52] F. S. Bergeret, A. F. Volkov, and K. B. Efetov, Odd triplet superconductivity and related phenomena in superconductor-ferromagnet structures, Rev. Mod. Phys. **77**, 1321 (2005).

[53] A. Di Bernardo, S. Diesch, Y. Gu, J. Linder, G. Divitini, C. Ducati, E. Scheer, M. G. Blamire, and J. W. A. Robinson, Signature of magnetic-dependent gapless odd frequency states at superconductor/ferromagnet interfaces, Nat. Commun. **6**, 8053 (2015).

[54] F. Parhizgar and A. M. Black-Schaffer, Diamagnetic and paramagnetic Meissner effect from odd-frequency pairing in multiorbital superconductors, Phys. Rev. B **104**, 054507 (2021).

[55] C. Triola, J. Cayao, and A. M. Black-Schaffer, The role of odd-frequency pairing in multiband superconductors, Ann. Phys. **532**, 1900298 (2020).

[56] L. Komendová and A. M. Black-Schaffer, Odd-Frequency Superconductivity in Sr_2RuO_4 Measured by Kerr Rotation, Phys. Rev. Lett. **119**, 087001 (2017).

[57] R. Sharma, S. D. Edkins, Z. Wang, A. Kostin, C. Sow, Y. Maeno, A. P. Mackenzie, J. C. S. Davis, and V. Madhavan, Momentum-resolved superconducting energy gaps of Sr_2RuO_4 from quasiparticle interference imaging, Proc. Natl. Acad. Sci. U.S.A. **117**, 5222 (2020).

[58] S. Hoshino and P. Werner, Superconductivity from Emerging Magnetic Moments, Phys. Rev. Lett. **115**, 247001 (2015).

[59] T. H. Lee, A. Chubukov, H. Miao, and G. Kotliar, Pairing Mechanism in Hund's Metal Superconductors and the Universality of the Superconducting Gap to Critical Temperature Ratio, Phys. Rev. Lett. **121**, 187003 (2018).

[60] X. Wu, W. Hanke, M. Fink, M. Klett, and R. Thomale, Harmonic fingerprint of unconventional superconductivity in twisted bilayer graphene, Phys. Rev. B **101**, 134517 (2020).

[61] H. G. Suh, H. Menke, P. M. R. Brydon, C. Timm, A. Ramires, and D. F. Agterberg, Stabilizing even-parity chiral superconductivity in Sr_2RuO_4, Phys. Rev. Research **2**, 032023(R) (2020).

[62] V. Grinenko, S. Ghosh, R. Sarkar, J.-C. Orain, A. Nikitin, M. Elender, D. Das, Z. Guguchia, F. Brückner, M. E. Barber, J. Park, N. Kikugawa, D. A. Sokolov, J. S. Bobowski, T. Miyoshi, Y. Maeno, A. P. Mackenzie, H. Luetkens, C. W. Hicks, and H.-H. Klauss, Split superconducting and time-reversal symmetry-breaking transitions in Sr_2RuO_4 under stress, Nat. Phys. **17**, 748 (2021).

[63] S. Benhabib, C. Lupien, I. Paul, L. Berges, M. Dion, M. Nardone, A. Zitouni, Z. Q. Mao, Y. Maeno, A. Georges, L. Taillefer, and C. Proust, Ultrasound evidence for a two-component superconducting order parameter in Sr_2RuO_4, Nat. Phys. **17**, 194 (2021).

[64] S. K. Ghosh, M. Smidman, T. Shang, J. F. Annett, A. D. Hillier, J. Quintanilla, and H. Yuan, Recent progress on superconductors with time-reversal symmetry breaking, J. Phys.: Condens. Matter **33**, 033001 (2021).

[65] V. Grinenko, D. Das, R. Gupta, B. Zinkl, N. Kikugawa, Y. Maeno, C. W. Hicks, H.-H. Klauss, M. Sigrist, and R. Khasanov, Unsplit superconducting and time reversal symmetry breaking transitions in Sr_2RuO_4 under hydrostatic pressure and disorder, Nat. Commun. **12**, 3920 (2021).

[66] J. Xia, Y. Maeno, P. T. Beyersdorf, M. M. Fejer, and A. Kapitulnik, High Resolution Polar Kerr Effect Measurements of Sr_2RuO_4: Evidence for Broken Time-Reversal Symmetry in the Superconducting State, Phys. Rev. Lett. **97**, 167002 (2006).

[67] G. M. Luke, Y. Fudamoto, K. M. Kojima, M. I. Larkin, J. Merrin, B. Nachumi, Y. J. Uemura, Y. Maeno, Z. Q. Mao, Y. Mori, H. Nakamura, and M. Sigrist, Time-reversal symmetry-breaking superconductivity in Sr_2RuO_4, Nature (London) **394**, 558 (1998).

[68] G. Luke, Y. Fudamoto, K. Kojima, M. Larkin, B. Nachumi, Y. Uemura, J. Sonier, Y. Maeno, Z. Mao, Y. Mori, and D. Agterberg, Unconventional superconductivity in Sr_2RuO_4, Physica B (Amsterdam) **289-290**, 373 (2000).

[69] J. R. Kirtley, C. Kallin, C. W. Hicks, E. A. Kim, Y. Liu, K. A. Moler, Y. Maeno, and K. D. Nelson, Upper limit on spontaneous supercurrents in Sr_2RuO_4, Phys. Rev. B **76**, 014526 (2007).

[70] C. W. Hicks, J. R. Kirtley, T. M. Lippman, N. C. Koshnick, M. E. Huber, Y. Maeno, W. M. Yuhasz, M. B. Maple, and K. A. Moler, Limits on superconductivity-related magnetization in Sr_2RuO4 and $PrOs_4Sb_{12}$ from scanning SQUID microscopy, Phys. Rev. B **81**, 214501 (2010).

[71] P. J. Curran, S. J. Bending, W. M. Desoky, A. S. Gibbs, S. L. Lee, and A. P. Mackenzie, Search for spontaneous edge currents and vortex imaging in Sr_2RuO4 mesostructures, Phys. Rev. B **89**, 144504 (2014).

[72] S. Kashiwaya, K. Saitoh, H. Kashiwaya, M. Koyanagi, M. Sato, K. Yada, Y. Tanaka, and Y. Maeno, Time-reversal invariant superconductivity of Sr_2RuO_4 revealed by Josephson effects, Phys. Rev. B **100**, 094530 (2019).

[73] S. NishiZaki, Y. Maeno, and Z. Mao, Effect of impurities on the specific heat of the spin-triplet superconductor Sr_2RuO_4, J. Low Temp. Phys. **117**, 1581 (1999).

[74] S. Nishizaki, Y. Maeno, and M. Zhiqiang, Changes in the superconducting state of Sr_2RuO_4 under magnetic fields probed by specific heat, J. Phys. Soc. Jpn. **69**, 572 (2000).

[75] K. Deguchi, Z. Q. Mao, H. Yaguchi, and Y. Maeno, Gap Structure of the Spin-Triplet Superconductor Sr_2RuO_4 Determined from the Field-Orientation Dependence of the Specific Heat, Phys. Rev. Lett. **92**, 047002 (2004).

[76] K. Deguchi, Z. Q. Mao, and Y. Maeno, Determination of the superconducting gap structure in all bands of the spin-triplet superconductor Sr_2RuO_4, J. Phys. Soc. Jpn. **73**, 1313 (2004).

[77] S. Kittaka, S. Nakamura, T. Sakakibara, N. Kikugawa, T. Terashima, S. Uji, D. A. Sokolov, A. P. Mackenzie, K. Irie, Y. Tsutsumi, K. Suzuki, and K. Machida, Searching for gap zeros in Sr_2RuO_4 via field-angle-dependent specific-heat measurement, J. Phys. Soc. Jpn. **87**, 0937031 (2018).

[78] C. Lupien, W. A. MacFarlane, C. Proust, L. Taillefer, Z. Q. Mao, and Y. Maeno, Ultrasound Attenuation in Sr2RuO4: An Angle-Resolved Study of the Superconducting Gap Function, Phys. Rev. Lett. **86**, 5986 (2001).

[79] I. Bonalde, B. D. Yanoff, M. B. Salamon, D. J. Van Harlingen, E. M. E. Chia, Z. Q. Mao, and Y. Maeno, Temperature Dependence of the Penetration Depth in Sr_2RuO_4: Evidence for Nodes in the Gap Function, Phys. Rev. Lett. **85**, 4775 (2000).

[80] E. Hassinger, P. Bourgeois-Hope, H. Taniguchi, S. René de Cotret, G. Grissonnanche, M. S. Anwar, Y. Maeno, N. Doiron-Leyraud, and L. Taillefer, Vertical Line Nodes in the Superconducting Gap Structure of Sr_2RuO_4, Phys. Rev. X **7**, 011032 (2017).

[81] M. Sigrist, Introduction to Unconventional Superconductivity, in *AIP Conference Proceedings*, Vol. 789 (AIP, Melville, NY, 2005), pp. 165–243.

[82] P. M. R. Brydon, D. F. Agterberg, H. Menke, and C. Timm, Bogoliubov fermi surfaces: General theory, magnetic order, and topology, Phys. Rev. B **98**, 224509 (2018).

[83] E. Jones, T. Oliphant, and P. Peterson, SciPy: Open source scientific tools for Python.

[84] O. Parcollet, M. Ferrero, T. Ayral, H. Hafermann, I. Krivenko, L. Messio, and P. Seth, TRIQS: A toolbox for research on interacting quantum systems, Comput. Phys. Commun. **196**, 398 (2015).

[85] P. Seth, I. Krivenko, M. Ferrero, and O. Parcollet, TRIQS/CTHYB: A continuous-time quantum Monte Carlo hybridisation expansion solver for quantum impurity problems, Comput. Phys. Commun. **200**, 274 (2016).

[86] H. U. R. Strand and S. Käser, TPRF: The two-particle response function tool box for TRIQS.

[87] ARPACK software.